Emerging Two-dimensional Tellurene and Tellurides for Broadband Photodetectors

Zihan Yan Hao Yang Zhuo Yang Chengao Ji Guangyu Zhang Yusong Tu Guangyu Du* Songhua Cai* Shenghuang Lin**

Z. Yan, Prof.G. Zhang, G. Du, Prof.S. Lin
Songshan lake materials laboratory, Dongguan 523808
Email Address: linshenghuang@sslab.org.cn
Z. Yan, H. Yang, Z. Yang, C. Ji, Prof.Y. Tu
College of Physics Science and Technology, Yangzhou University, Jiangsu 225009, China.
Email Address: ystu@yzu.edu.cn
G.Du, Dr.S.Cai
Department of Applied Physics, The Hong Kong Polytechnic University, Hunghom, Kowloon, Hong Kong 999077
Email Address: guangyu.du@connect.polyu.hk; songhua.cai@polyu.edu.hk

Keywords: *Tellurene, Tellurides, Photodetectors, Heterostructure, Optical and Electronic properties*

As for the stylish two-dimensional (2D) functional materials, the intriguing properties of tellurene and tellurides are gradually recognized in high environmental stability, tunable narrow bandgap and lower thermal conductivity, *etc.*, which has aroused the great interest of the researchers. These properties of such materials formed the basis for relatively newfangled scholarly fields involving advanced topics especially for broadband photodetectors. Integrating the excellent properties of many 2D materials, tellurene/tellurides-based photodetectors show great flexibility, higher frequency response or faster time response, high signal-to-noise ratio, and so on, which makes them leading the frontier of photodector research. To fully understand the excellent properties of tellurene/tellurides and their optoelectronic applications, the recent advances on tellurene/tellurides based photodetectors are maximatily summarized. Benefiting from the solid research in this field, the challenges and opportunities of tellurene/tellurides for future optoelectronic applications are also discussed in this review, which might provide possibilities for the realization of state-of-the-art high-performance tellurene/tellurides based devices.

1 Introduction

The emergence of graphene in 2004[1] has made two-dimensional (2D) materials an enduring focus of research over the years. Many 2D materials, such as germanene, silicene, borophene and phosphorene, exhibit excellent electronic, optical, and thermodynamic properties.[2, 3, 4, 5] The in-depth researches on 2D materials will provide new approaches to the manufacture of devices in a wide range, thus exerting tremendous effects on materials science, chemistry, physics, biology, biomedicine and so on.[6, 7, 8, 9, 10, 11] Over decades, graphene has been widely investigated and applied in wastewater treatment,[12] (bio)sensors,[13, 14] composite materials[15] and other fields due to its excellent thermal and mechanical properties.[16, 17] Its zero-bandgap characteristics, however, significantly limits the practical applications in optoelectronics. Then, the transition metal dichalcogenides (TMDs) came on the scene as the first graphene descendants, which are semiconductive essentially and are more promising to be fabricated into ultra-small low power devices compared with graphene, with the potential to be deposited onto flexible substrates at the same time.[18, 19, 20] In contrast, another 2D material, black phosphorus (BP), exhibits the incomparable advantages over graphene and TMDCs, such as optical anisotropy,[21] tunable bandgap[22] and so on. The tunable bandgap enables BP to suppress dark current effectively, thus enabling high signal-to-noise ratio light detection.[23, 24, 25, 26] However, the preparation of BP is more difficult, and BP exhibits poor stability in the ambient environment.[27] Hence, there is a pressing need to develop a new material that has both tunable bandgap and outstanding environmental stability for photodetection and other purposes.

As a metalloid element of group-VI, tellurium (Te) is famous for its excellent properties from various perspectives, such as piezoelectricity,[28] photoconductivity,[29] and thermoelectricity.[30] In 2017, through first-principles calculations, researchers successfully predicted the 2D structure of tellurium,[31] named tellurene, which has three configurations, the stable 1T-MoS_2-like (α-Te) structure, as well as the metastable

tetragonal (β-Te) structure and the 2H-MoS_2-like (γ-Te) structures. They also measured the electron and hole mobility of the three configurations through the acoustic phonon limited method to find out that α-Te and β-Te have carrier mobility of hundreds to thousands of $cm^2V^{-1}s^{-1}$ at room temperature. Subsequently, Wang *et al.*[32] successfully prepared high-quality tellurene using a substrate-free solution process, with a new member added to the 2D material family.

Compared with other 2D materials, in both theoretically and experimentally, tellurene shows high environmental stability,[31, 33] tunable bandgap,[34] and lower thermal conductivity,[35] for which they have aroused great interest among the researchers, especially the tunable bandgap character grants such material system spectral tunability with a wide operating spectral range for multispectral photodetectors that are sensitive to visible, ultraviolet, near-infrared, and far-infrared, thus broadband photodetectors, the key figures-of-merit of which contain external quantum efficiency (EQE), detectivity (D^*) and responsivity (R) that serve as a prevailing platform for an impartial comparison among broadband photodetectors.[36, 37, 38, 39] In addition, tellurene has different physical configurations, which makes tellurene-based compounds have more types and more functionalities. Since the discovery of tellurene, people have conducted a lot of studies on tellurene and its compounds serving as photoelectric sensors.[38, 40, 41] For instance, an unusual photoresponse behavior of Te nanosheet based on the modulation of thickness has been reported.[40] When the thickness of the Te nanosheet is thinner than 5 nm, the negative behavior of the photoresponse appears while increasing the thickness can make the behavior become positive. Additionally, an intriguing synthesis strategy for the transformion of 1D tellurium nanowires into 2D tellurene nanobelts was proposed, which has been proved to have a microwave-enhanced effect on photodetector application.[41] Moreover, on the flexible mica sheet, a special 2D hexagonal tellurium nanosheet was prepared by van der Waals epitaxy (vdWE), it can still exhibit efficient photoresponsivity after bending over 100 times, which indicates the considerable potential for applications in flexible and wearable optoelectronic devices.[42] Meanwhile, continuous attention has been paid to the preparation and applications of tellurides. Compared with tellurene, tellurides have different energy bands and electrochemical properties, such as higher electron mobility and conductivity.[43, 44, 45] With a series of tellurides that have been derived (like SnTe, $PtTe_2$, $MoTe_2$, GeTe, GaTe), the superior photoelectronic properties of tellurides have provided new solutions to the design of new photodetectors with better performance. For example, a $MoTe_2$/graphene heterostructure photodetector has been proved to be promising in the efficient detection of near-infrared (NIR) light.[46] Besides, the $PtTe_2$/Si Schottky junction exhibits a high specific detection rate and an excellent room-temperature infrared-imaging capability.[47] Therefore, a comprehensive understanding as to the physical properties of tellurene and tellurides is essential for further promoting these materials from the laboratory to industrial production. For these reasons, this review spotlights the applications and development of tellurene and tellurides in the field of photodetectors, with the hope to sort out the research progress made in this field in recent years and present it to wide range readers as much as possible. We start by introducing the electronic and optical properties of tellurene in detail. Then, the applications of tellurene/tellurides-based photodetectors are listed. Finally, a brief discussion is conducted about the prospects and challenges of photodetectors based on 2D tellurene and tellurides are briefly discussed.

2 Electronic and optical properties

We have already discussed various excellent properties exhibited by tellurene, such as high carrier mobility, outstanding environmental stability, low thermal conductivity, tunable bandgap, and so on. Among them, the most distinctive and striking properties are the high carrier mobility and tunable bandgap, which will make its electronic and optical performances significantly distinguishable from other 2D materials. In this section, we have made a detailed summary as to the electronic and optical properties of tellurene.

2.1 Electronic properties

2D materials usually have excellent electronic properties due to their extraordinary structures. As a new member of the 2D material family, tellurene possesses most of the properties that other 2D materials have. Moreover, it has high carrier mobility, thickness-dependent bandgap, special interlayer coupling, and splendid photoelectronic performance, which provides a strong supports for the development of tellurene-based photodetectors. In this subsection, we have reviewed a series of first principles calculations and experiments to summarized the electronic properties of tellurene.

2.1.1 Structure of tellurene

The unique spiral structure and inherent multivalent properties of tellurene are significantly different from the notable 2D materials such as graphene and silicene. As we mentioned above, tellurene has three different configurations (1T-MoS_2-like (α-Te), tetragonal (β-Te) and 2H-MoS_2-like (γ-Te) structures).[31](see **Figure 1**a-c) The average cohesive energy of α-Te (2.62 eV/atom) is much higher than β-Te (2.56 eV/atom) and γ-Te (2.46 eV/atom), as a result of which α-Te shows better stability. It is worth mentioning that monolayer β-Te has a tendency to be transformed into monolayer α-Te not only for the higher average cohesive energy, but also for more CLQBs (in the two-layer β-Te, each Te atom has 4/3 CLQBs, but the monolayer has only 2/3 CLQBs),[34] and the definition of CQLB will be given later. At finite temperatures, both the phonon calculations and the *ab initio* molecular dynamics simulations (AIMD) were performed to examine the thermodynamic and dynamic stability of tellurene.[31] For details, all of three structures are dynamically stable. At room temperature, α- and β-Te are very stable, but γ-Te cannot stay stable even at about 200 K.

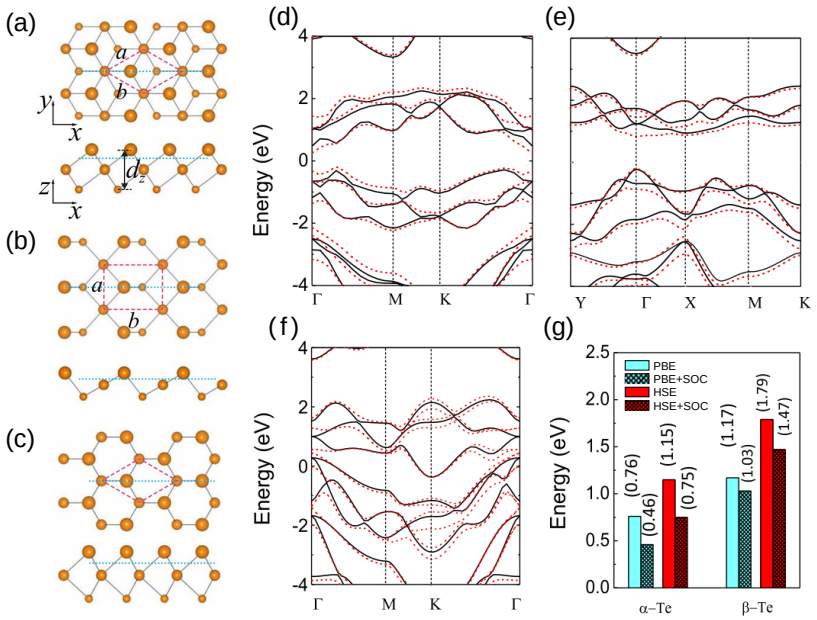

Figure 1: The configurations (a-c) and band structures (d-f) of α-, β-, and γ-Te, respectively. Note: The band diagram is calculated by PBE without SOC (solid line) and with SOC (dashed line). g) bandgaps obtained within the PBE (PBE + SOC) and HSE (HSE + SOC) schemes.[31] Copyright 2017, American Physical Society.

In addition, the multivalence of Te also makes the properties different from Te with different layers. Actually, both metallic and metalloid characters are shown in Te. The central-layer Te atoms behave as more of a metal, whereas the outer-layer Te atoms are more of a semiconductor. This may be because the Te atoms in the center layer have higher coordination numbers n_c (for α- and γ-Te, $n_{c-central-layer-Te} = 6$, while β-Te is 4) and are bonded with outer-layer Te atoms through metal-ligand-like bond. A further Bader charge analysis confirmed the metal-like properties of the central-layer Te. Based on Bader charge analysis, in α-, β- and γ-Te, the amount of charge transfer from the central atom to the outer atom is

0.41, 0.11, and 0.29 eV respectively. The energy band of tellurene is more interesting. The α-, β-Te with indirect bandgaps (0.76 eV for α-Te and 1.17 eV for β-Te) are semiconductors, while γ-Te exhibit metallic properties. In Figure 1d,e, it can be seen clearly that for α- and β-Te, the spin-orbit coupling (SOC) induces the transition from indirect to near-direct and direct bandgap at the Γ point. Such an indirect-to-direct bandgap transformation of α- and β-Te greatly increases its light absorption, which may broaden the scope of applications for tellurene in photoelectronics and photon detection. Meanwhile, the optical anisotropy exhibited by β-Te shows its potential of being used as polarization optical sensors.

2.1.2 Bandstructures and couplings of few-layer Te

There are many ways of interlayer coupling in 2D materials. Different coupling ways of 2D materials can lead to different properties. To some extent, they are one of the reasons why the material exhibits certain properties. Graphite sheets are generally formed by weaker SOC, which belongs to the coupling of van der Waals interaction, while tellurene, BP,[49, 50] PtS_2[51] and $PtSe_2$[52] are carried out by the so-called covalent-like quasi-bonding (CLQB). The interlayer coupling ways of Te do affect the nature of the few-layer Te, which causes the transition from indirect to near-direct and direct bandgap (see Figure 1d,e).

Furthermore, the bandgap is a vital characteristic of 2D materials, because it will have a significant impact on the electronic and optical properties of these materials. **Figure 2**c-g presents the band structure of Te from 2 to 6 layers respectively. Both previous experiments and first-principles calculations show that bulk Te is a semiconductor with a direct energy band around 0.31–0.34 eV.[53, 34] Moreover, the relationships between indirect bandgaps, the position of conduction band minimum (CBM) and valence band maximum (VBM), and the thickness of sample were calculated by hybrid (HSE06) functionals and vdW-DF with or without SOC (see **Figure 3**a,b). Regardless of whatever functionals or methods are used, and whether SOC is considered, the relationships between them show the same tendency. The number of layers increases, but the bandgap decreases. The bandgap of few-layer Te is reduced from 1.17 eV (2L) to 0.95 eV (3L), 0.83 eV (4L), 0.72 eV (5L), and 0.66 eV (6L) respectively when HSE06+SOC is used. From Figure 3b, it is seemingly attributable to the increase in the number of Te layers that significantly increases VBM, but CBM has not been severely affected.[34]

Besides, to better understand the different orbital contributions to the electronic states in Te, the total density of states (TDOS) and partial density of states (PDOS) were considered and calculated by PBE function.[48] From Figure 2i, it can be found out that both VBM and CBM are dominated by p orbitals, while the level of s-d mixing in VBM and CBM is dependent on the state location. Moreover, the movement of the VBM to the Fermi level is not asymptotic but exhibits odd-even quantum confinement character. Figure 3c-f show the differential charge density (DCD) of DCD-dbC (double Te atomic chains) and DCD-2L (bilayer β-Te). It can be found out that charge reduction is near one Te atoms and accumulation between two Te atoms, which shows the covalent properties of these interactions. Also, the partial charge density which can reflect the spatial distribution of the bilayer-β-Te wave function is shown in Figures 3g–j. As can be seen form them, at the H' point (see Figure 2 (b)), the rectangle in Figure 3g (state VB4) shows interlayer bonding states while (h) (state VB1) shows anti-bonding states. As previously observed in BP,[49, 50] PtS_2[51] and $PtSe_2$[52], this bonding occupying both the bonding and anti-bonding states is CLQB.

2.1.3 Carrier mobility of tellurene

For semiconductor materials, carrier mobility is a parameter that has to be considered carefully. It can clearly reflect the moving speed of carriers, that is, electrons and holes, in a solid material under an external electric field. This also determines whether it can be used for the manufacture of electronic equipments in a wide range. For a long time, people have been committed to exploring materials with high carrier mobility, which can provide higher frequency response or faster time response and significantly improve the performance of the photodetectors. Hence, the acoustic phonon limited method has been adopted to examine the carrier mobilities of α- and β-Te at 300 K.[31] At the same time, the effective masses and

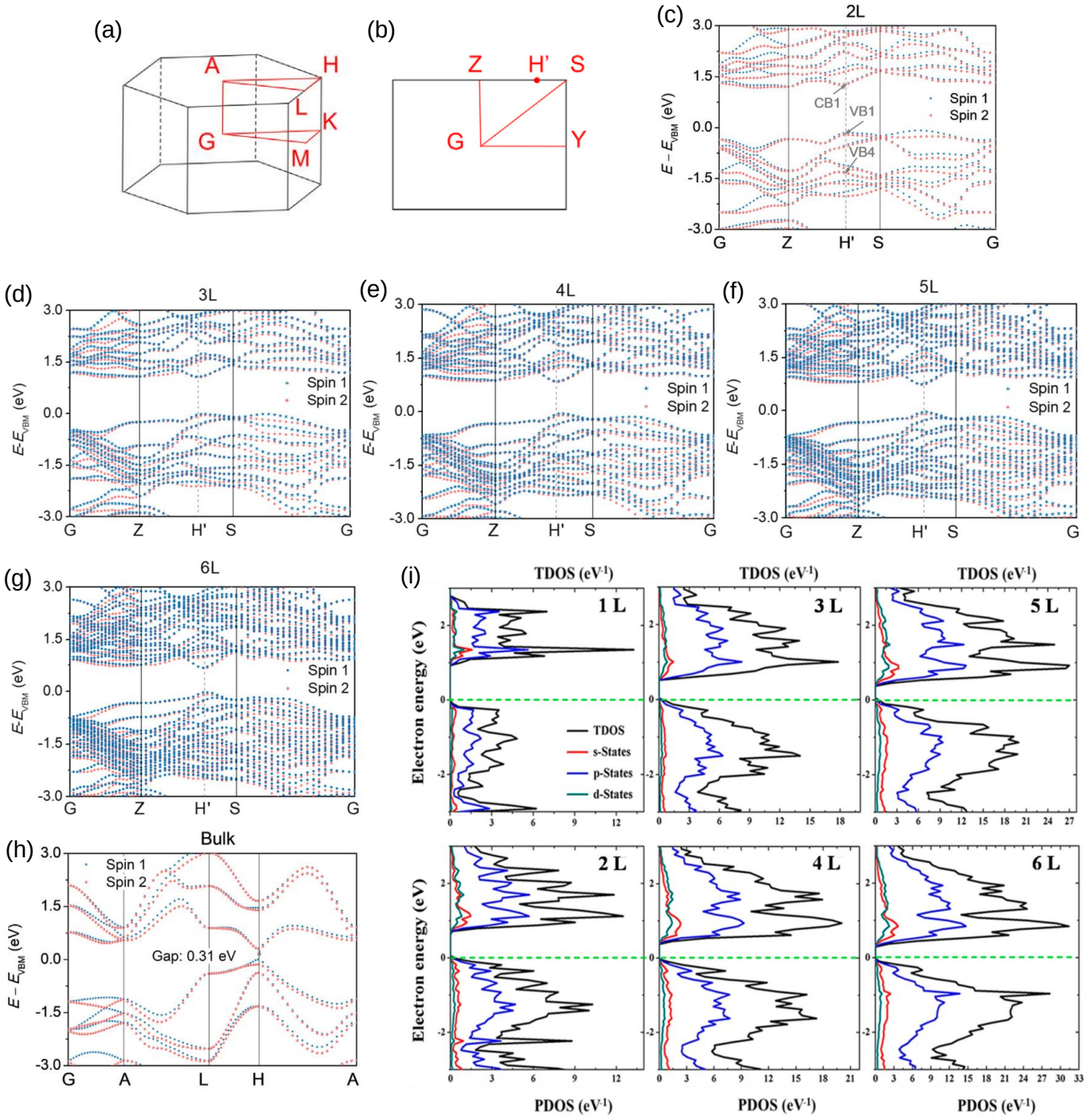

Figure 2: a,b) Brillouin zones of Bulk and few-layer β-Te. c-h) Bandstructures of 2 to 6 layer (2L–6L) β-Te and bulk, respectively.[34] Copyright 2018, Elsevier. i) TDOS and PDOS of tellurene in different layers calculated by the PBE+SOC.[48] Copyright 2019, Sang *et al.*

carrier mobility of monolayer 2H-MoS_2 have also been calculated and listed for the purpose of comparison. From the **Table 1**, it can be seen that the effective masses of α- and β-Te are relatively smaller compared to monolayer 2H-MoS_2. Also, the carrier mobilities of both electron (μ_e) and hole (μ_h) are much higher than 2H-MoS_2, falling within a wide range of 0.05–2.09$\times10^3$ $cm^2V^{-1}s^{-1}$ (for electron) and 0.45–1.98$\times10^3$ $cm^2V^{-1}s^{-1}$ (for hole), respectively. It is worth noting that the different effective masses result in the asymmetric mobility of electrons and holes, as reflected in β-Te. Therefore, β-Te shows the anisotropy of electron and hole mobility in the y direction.

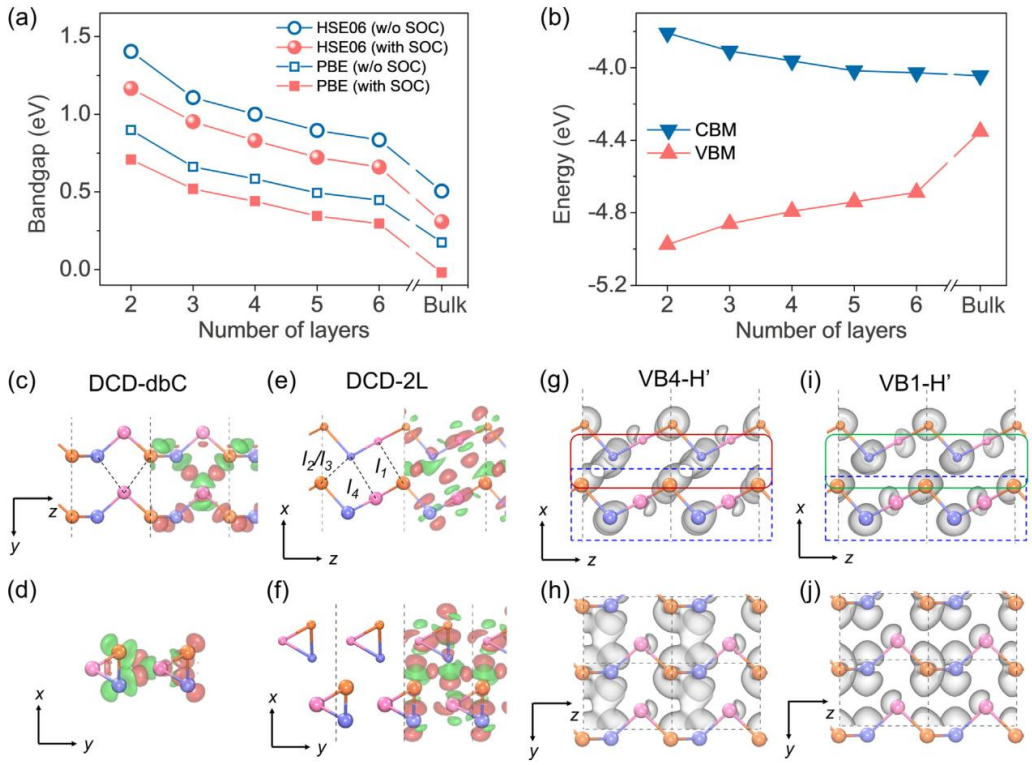

Figure 3: Interlayer couplings of few-layer β-Te. a,b) The relationship between bandgap, CBM, VBM, and sample thickness. c-f) Differential charge density of DCD-dbC (double Te atomic chains) and DCD-2L (bilayer β-Te). g-j) Visualized wavefunctions for g,h) VB4-H' and i,j) VB1-H'.[34] Copyright 2018, Elsevier.

Table 1: The carrier mobilities μ and effective masses m^* of α-, β-Te, and 2H-MoS_2, calculated by the PBE+SOC. (x) and (y) represent the armchair chain and zigzag chain directions respectively. Data from Ref[31]

	$m^*(m_e)$		$\mu(10^3\ cm^2V^{-1}s^{-1})$	
	Electron	Hole	Electron	Hole
α-Te	0.11	0.17	2.09	1.76
β-Te	0.83(x)	0.39(x)	0.05(x)	1.98(x)
	0.19(y)	0.11(y)	0.10(y)	0.45(y)
2H-MoS_2	0.47	0.58	0.08	0.29

2.1.4 Strained tellurene

Many ways that can modulate the characteristics of 2D materials have now been proposed, such as substrates regulation,[54, 55, 56] stacking,[57, 58, 59] atomic doping,[60] and strain,[54, 61, 62, 63] *etc.* Among them, the strain has received widespread attention as one of the most direct ways of influence, such as strain-dependent adsorption energy of the benzene-graphene system.[54] The compressive strain will increase the adsorption energy of benzene on graphene. In fact, not only does it affect the adsorption energy, applying external stress can also effectively adjust the electronic properties of 2D materials. At the moment, strain has become an easy-to-implement routine method for designing electronic properties of semiconductors.[61, 62]

The tension between Te layers will reduce the direct bandgap, but compression will induce Te to show a direct-to-indirect bandgap.[64] **Figure 4**a shows the change in bandstructures of β-Te when biaxial strain is applied. It is easily observable that when tension is applied, from $\varepsilon = 0\%$ to 6%, tellurium still maintains the characteristics of the direct bandgap. The energy of VBM does not change significantly, while CBM gradually shifts down towards the Fermi Level, which makes the bandgap gradually shrink. The bandgap is only 0.86 eV when the tension is applied to 6%. More notably, it can be seen from Figure 4a that the CBM shifts from Γ to X. When ε = -2%, the applied compression strain induces a transition from

the direct bandgap to the indirect bandgap. As the compression strain continues to increase, the energy of CBM will gradually shift down towards the Fermi Level, but Te is remains a semiconductor with an indirect bandgap. Eventually, when the compression strain is increased to ε = -10%, tellurium even exhibits metallic characteristics. In fact, along different directions, the impact of strain on the electronic properties of tellurene exhibits anisotropy. Figure 4b shows the impact of uniaxial strain on the tellurene bandgap in the zigzag (blue line) and armchair (black line) directions. The zigzag direction presents an effect similar to the biaxial strain, and the compressive strain clearly changes the bandgap and its electronic properties. However, the strain in the armchair direction does not lead to a significant change in the bandgap. In addition, the tensile strain has little effect on the tellurene band structure. In contrast, the armchair direction and biaxial strain change more significantly than the zigzag direction.[64]

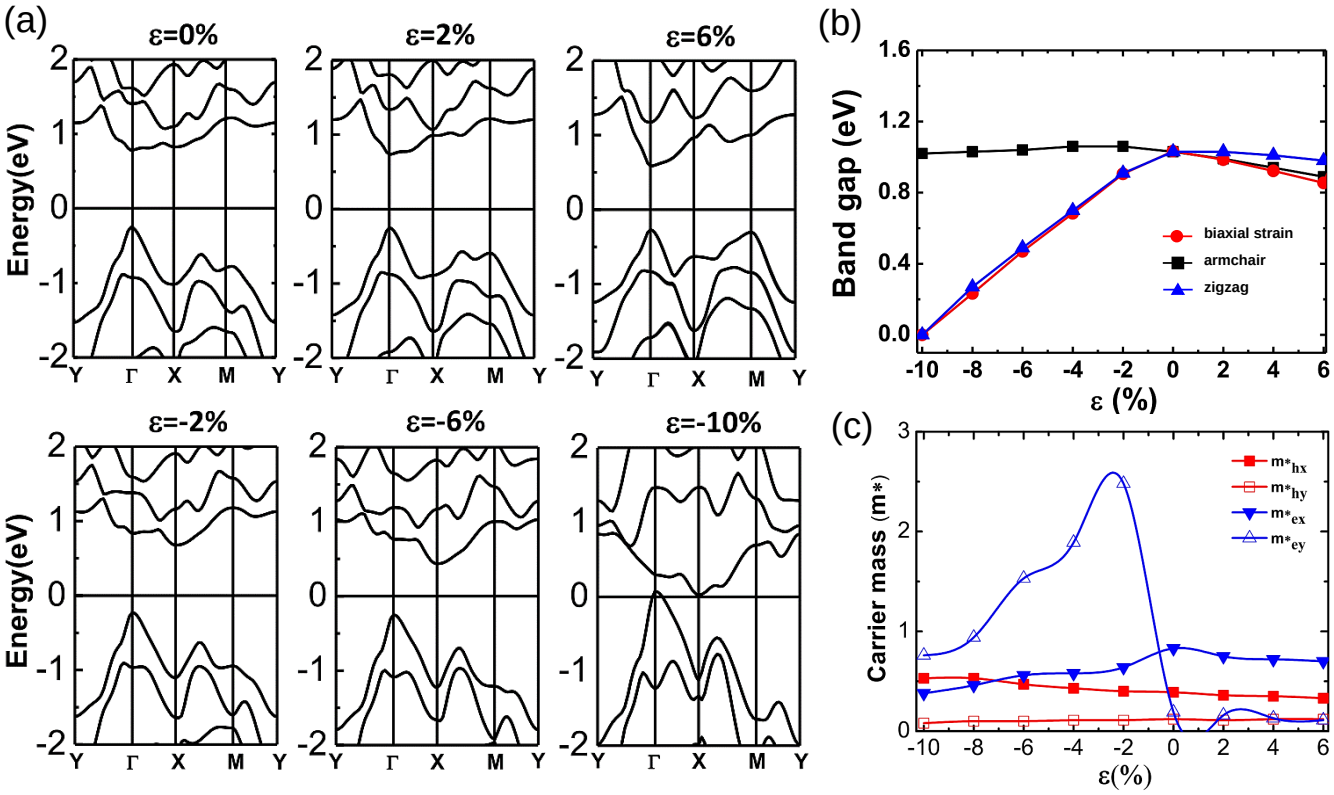

Figure 4: a) The band structures of 2D Te under different biaxial strain (from ε = -10% to 6%) with SOC. b) Variations of bandgap under different strain. c) Variations of hole and electronic effective masses with respect to the biaxial strain for tellurene.[64] Copyright 2016, Zhu *et al.*

As mentioned earlier, effective mass is also an important influencing factor for carrier mobility. In fact, effective electron/hole masses are also affected by the strain of tellurene. Figure 4c shows the relationship between the effective mass of electrons and holes and the biaxial strain of β-Te. Compressive strain significantly changes the effective mass of electrons, thus causing m^*_{ey} to rise sharply to 2.48 m_e at ε = -2% (it has to be said that this jump greatly changes the electronic conduction properties of tellurene). With continued compression until ε = -10%, and the m^*_{ey} will gradually decrease. Compared with the previous energy bandstructures, the change of m^*_{ey} is also consistent with the results of CBM shifting from Γ to X, thus causing a transition from the direct bandgap to the indirect bandgap. Also, the m^*_{ex} decreases from 0.83 m_e (ε = 0%) to 0.36 m_e (ε = -10%). Additionally, neither the tensile strain nor the compressive strain has substantial impact on the effective mass of the hole. Later, similar results were obtained by Ma *et al.*, confirming the effect of strain engineering on the electronic properties of β-Te.[62]

Dong *et al.* showed that due to its inherent structural characteristics, β-Te exhibits extremely pronounced anisotropy in stress-strain curves, Poisson's ratio, and Young's modulus.[61] β-Te can withstand extremely high strains.(∼35% in the zigzag direction and ∼36% in the armchair direction) The Young's

modulus of β-Te is 55 GPa in the zigzag direction and 27 GPa in the armchair direction, which is close to the results of Ma *et al.*[62] The very high critical strain and the small Young's modulus imply that β-Te has good flexibility. Considering again its high anisotropic carrier mobility, β-Te becomes a promising candidate for flexible nanoelectronics.

2.2 Optical properties

The research on the optical properties of tellurene has been extensively carried out in recent years.[65, 66, 67] Tellurene is an excellent potential material for photodetector applications, the optical properties of which largely determine its applicability in photodetection. In this section, an overview is presented of the main optical properties of tellurene. The optical properties of tellurides and the performance of tellurene/telluride-based photodetectors will be described in detail in the following section.

Experimentally, relatively stable α- and β-Te are easier to be prepared, so that there are more studies focusing on the optical properties demonstrated by these two phases of tellurene.[70, 71] Studies have shown that both α- and β-Te exhibit a positive absorption response to light. At the same time, the light absorption coefficient (absorption efficiency) of the few-layer α- and β-Te will decrease when its thickness increases, which results from the layer-dependent energy band, strong interchain coupling, and the interlayer coupling caused by interlayer electron hybridization. Further analysis shows that α- and β-Te exhibit good optical responses to infrared to visible light and visible light to ultraviolet light, respectively. Under laser irradiation with the wavelengths of 512 and 382 nm, the light absorbance of the few-layer α-Te shows the layer-dependent behavior, and the absorption rate in each layer of the bilayer α-Te is almost 1.65 times (512 nm) and 2 times (382 nm) higher than the bulk Te, respectively. The light absorption rate of few-layer β-Te at 175 nm exceeds 0.5×10^5 cm^{-1} and is gradually extended to the visible light region, with the highest absorption achieved for the blue-violet visible region. The bulk Te exhibits the highest absorption intensity in the 140 nm ultraviolet region.

In experiments, Raman spectrum is one of the most important means to verify the types and properties of experimentally prepared materials.[72, 73] For the 2D tellurene whose properties are significantly influenced by the number of layers, the determination of Raman spectra can be conducive to the preparation and study of it. The Raman spectral line of 2D Te at room temperature shows that the tellurene nanosheets with a greater thickness greater than 20.5 nm exhibit three different modes of Raman activity modes located at approximately 92, 121, and 125 cm^{-1} (see **Figure 5**d), respectively.[68] As the thickness of the few-layer Te decreases, the electro-optic effect of the 2D Te lattice diminishes. Besides, along with the potential energy of the phase change, the Raman peak of the tellurene with a thickness of 9.1 nm shows the E_1 longitudinal (LO) mode. In addition, the reduction in thickness also leads to the obvious peak shift of the Raman spectrum. As the layer of β-Te decreases, the Raman peak undergoes obvious low-frequency to high-frequency movement (The A_g and B_g modes are vibrational modes in the parallel/perpendicular atomic layer direction, respectively.). Such changes are caused by the symmetrical distribution of the structure, the changes in the electronic energy bandstructure, and the structural phase caused by the reduced number of layers.

On the other hand, the effect of strain on the optical performance of Te cannot be ignored. As revealed by the studies on the Raman spectra of tellurene affected by strain, the uniaxial strain along the c-axis of the structure can cause Raman spectra to show obvious changes, while the strain along the a-axis of the 2D Te will not cause any changes to Raman spectra.[69] The Lorentzian function was relied on to fit the Raman spectra, so as to obtain the peak frequency of each mode at different strain magnitudes. Both tensile and compressive strains change the Te-Te atomic distances, which affects their interactions. The compressive strain applied to Te along the c-axis causes a blue shift in both the A_1 and E^2 modes, with the slopes of 1.1 cm^{-1}%$^{-1}$ and 0.9 cm^{-1}%$^{-1}$, respectively, whereas uniaxial tensile strain causes a red shift in A_1 and E^2, with a slopes of 1.0 cm^{-1}%$^{-1}$ and 1.2 cm^{-1}%$^{-1}$, respectively. No measurable Raman shift was observed in the E^1 mode, nor did strain in the c-axis cause any change in the position of the E_1 peak, which is attributed to the low sensitivity of the E^1 mode to deformation in the c-axis. The strain in the a-axis did not cause a shift in the mode peak, which is a further evidences not only the anisotropy of the 2D Te, but also the fact that the 2D Te conforms to weak van der Waals interaction in the a-axis and that

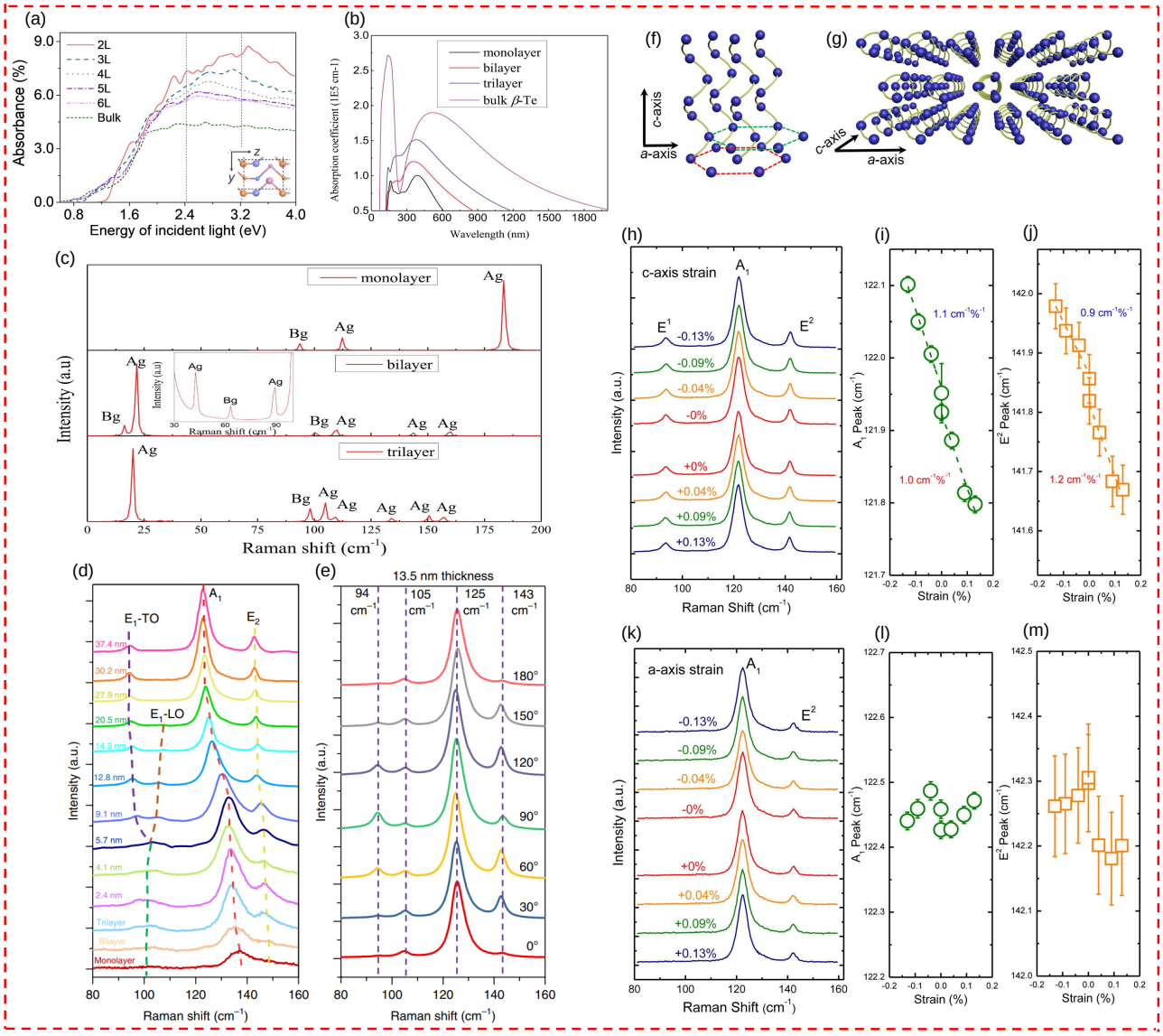

Figure 5: a) Absorbance per layer of few-layer β-Te with incident light along the y direction.[34] Copyright 2018, Elsevier. b) Optical absorption coefficients of β-Te with different layers. c) Raman spectra of β-Te calculated by DFPT with 514.5 nm laser illumination.[33] Copyright 2017, IOP Publishing Ltd. d) Raman spectra of 2D Te with different thicknesses. e) Angle-resolved Raman spectra of 13.5 nm flake.[68] Copyright 2018, Nature Publishing Group. f,g) Lattice structure of Te. h-m) Raman spectra (h,k) and Raman shift of (i,l) A_1 and (j,m) E^2 modes of 2D Te flake with strains in c-axis (for h-j) and a-axis (for k-m).[69] Copyright 2017, American Chemical Society.

strain does not affect the Te interatomic distance.

In terms of light response mechanism, tellurene is similar to most materials intended for photoelectric detection. One type of mechanism is free carrier excitation. Caused by optical transition, it includes the photoconductive effect, the photovoltaic effect, and the photogating effect.[74] The other is caused by thermal effects, such as the bolometric effect and photothermoelectric (PTE) effect.[75] The photodetectors working with the photovoltaic effect often form a *p*-*n* structure through heterostructure by chemical doping and form a photovoltaic voltage by dividing photogenerated electron-hole (e-h) pairs. The output curves of these devices under dark and light conditions are nonlinear with rectification characteristics. Besides, they are able to operate at zero or reverse bias while maintaining very low dark currents and high quantum efficiencies. The applications of reverse bias can also accelerate the production of photogenerated carriers, thus leading to large photoconductive gains, which suggests that such devices are of high value in the field of weak light detection. The photoelectric effect and the thermal radiation effect are both affected to some extent by the device fabrication process. The photodetectors based on the photoelectric effect are often considered as light-generated free electron-hole pairs caught in a trap state, thus allowing the charged trap state to act as a localized floating gate that strongly modulates the channel conductance. For example, the GaTe nanosheet photodetector, which will be mentioned later, has more trap states due to its manufacturing process, which makes the device unfit for use in an air environment, despite the excellent photocurrent linearity in vacuum.

3 Applications

A photodetector, also known as photosensor or O/E convertor, is a type of device which converts optical signals into electrical signals. Photodectors have been widely used in such settings as industrial automatic control, missile guidance and infrared thermal imaging, *etc.* Heretofore, over hundreds of photodetectors are conceived and manufactured based on 2D materials. As the research on tellurene and tellurides deepens, there have been many projects implemented to take advantage of the excellent properties exhibited by tellurene and tellurides to develop photodetectors, such as large-scale and environmental stability. Herein, we have reviewed the research of photodetectors based on tellurene or tellurides ($MoTe_2$, $PdTe_2$, $PtTe_2$, WTe_2, GeTe, SnTe, GaTe) in recent years.

3.1 Tellurene photodetector

As a *p*-type helical semiconductor, at room temperature, bulk Te has a narrow bandgap of 0.35 eV. Various excellent physical properties, such as high thermoelectricity,[30] photoconductivity,[29] nonlinear optical response,[76] and piezoelectricity,[28] make it an excellent candidate in such applications as infrared acoustooptic deflectors,[77] solar cells,[78] gas sensing,[79] photoconductors,[80] and field-effect transistors.[81] When Te is fabricated down to the nanoscale, its physical properties are remarkably distinct from those of bulk Te. According to recent studies, tellurene has the following advantages in performance and process: (1) the bandgap of tellurene can be adjusted by thickness and the operational wavelength covers visible to mid-infrared wavelengths; (2) it demonstrates unique polarization sensitivity and ultra-fast responsiveness; (3) it has a good electron modulation ratio ($\sim 10^5$–10^6) and can be consumed by adding a reverse electric field; (4) tellurene is stable under air and room temperature conditions and does not require additional encapsulation techniques; (5) the chain structure of tellurene leads to a long carrier lifetime; (6) It can be mass-produced by substrate-free, low-cost solution treatment and integrated in a large area. In summary, as an emerging 2D material, tellurene combines such advantages as tunable bandgap, polarization sensitivity, high carrier mobility, long carrier lifetime, excellent environmental stability, and easy preparation.

In 2018,[32] the successful preparation of high-quality, large-area, thickness-tunable 2D tellurium by a substrate-free solution process rekindled widespread interest among researchers. Thereafter, the relevant electronic and optical properties of the few-layer tellurene were calculated by first principles.[34, 48] Unlike the monolayer (1 L) structure, the bandgap of few-layer tellurene (2–6 L) changes from direct to indirect, and it can be adjusted in the range from 1.0 eV (1 L) to 0.3 eV (6 L). The results clearly

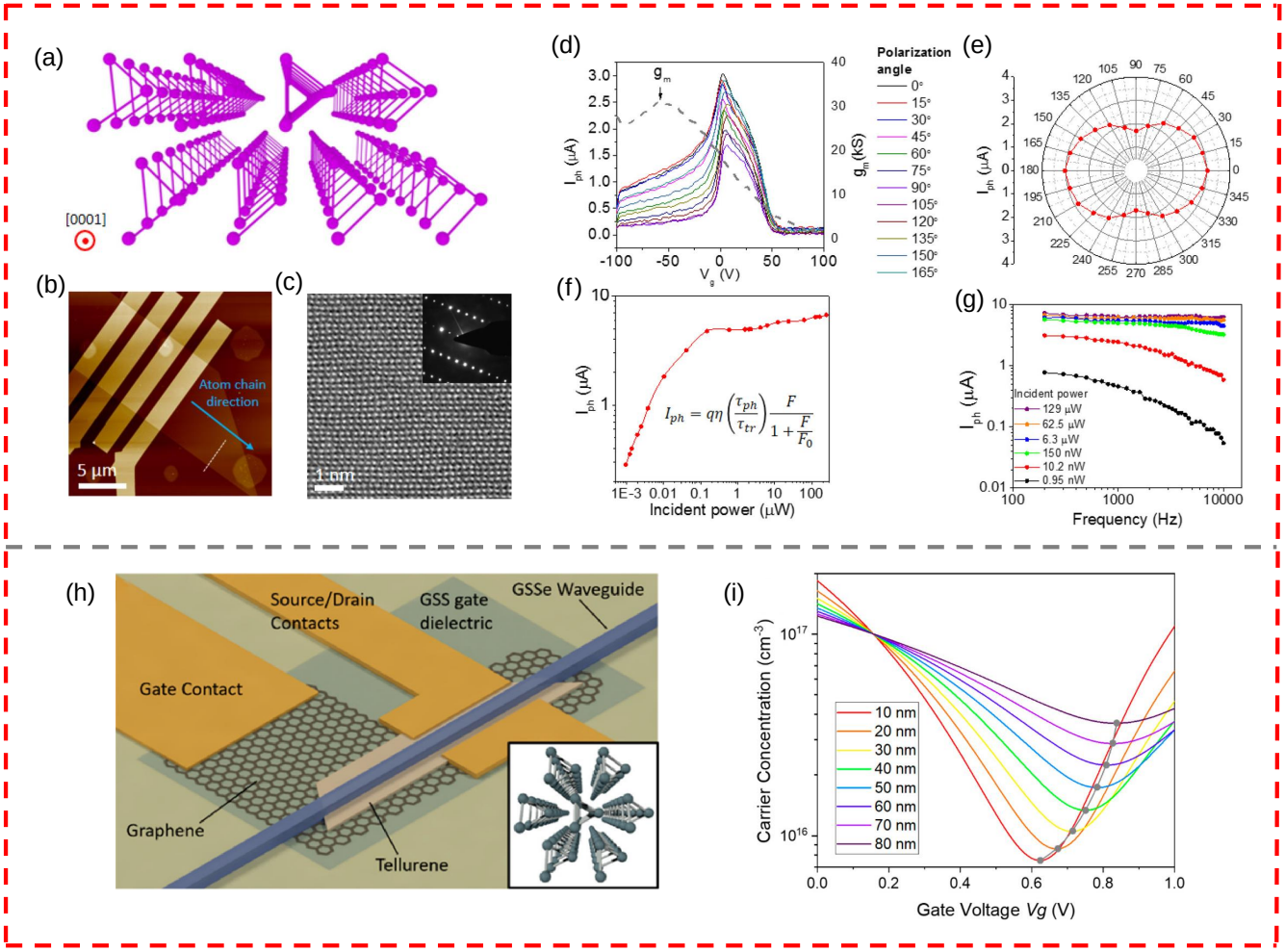

Figure 6: a) Schematic illustration of the crystallographic structure of tellurene. b) AFM image of back-gate tellurene FET. c) TEM image of tellurene (inset: the SAED pattern). d-g) Tellurene photodetector operating at 520 nm. d) Gate-dependent photocurrent (left axis) and channel trans-conductance (g_m, dash gray line, right axis) measured at different polarization angles (V_{ds}= 1 V). e-g) Dependence of the photocurrent with polarization angles, power dependence of photocurrent, and photocurrent versus modulation frequency under various incident powers (V_g= 5 V and V_{ds}=1 V), respectively.[38] Copyright 2019, American Chemical Society. h) Schematic illustration of waveguide integrated tellurene photodetector. i) Effective carrier concentration under different gate voltages in tellurene flakes of different thicknesses.[82] Copyright 2019, American Chemical Society.

demonstrate the layer dependence of the electronic and optical properties exhibited by tellurene. The significant variation in the electronic energy bandstructure and excellent absorption properties of tellurene has promising applications in ultra-high-speed transistors and photodetector devices in the near-infrared, ultraviolet and visible regions. For example, in the field of high-gain bandwidth photodetectors, air-stable and hydrothermally-synthesized 2D tellurium nanosheets have been used for broadband and ultra-sensitive light detection.

Figure 6a presents a schematic diagram of the crystal structure possessed by tellurene. Each Te in the chain is covalently bonded to its two nearest neighboring Te atoms, thus forming triangular helical-chains, and the helical-chains are arranged in parallel in the [0001] direction. Figure 6b illustrates a synthesized tellurene nanoflake with four electrodes. From Figure 6c, it can be seen that the single-crystal nature of the tellurium has been successfully revealed through the images of high-resolution transmission electron microscopy (TEM) and the patterns of selected area electron diffraction (SAED). The crystal plane spacing is 1.9 Å([1210] planes) and 2.8 Å([0001] planes), which is consistent with the calculation results of DFT.[34, 83] Based on the physical properties of tellurene, Shen *et al.* reported the study of a tellurium-based photodetector operating in the wavelength range from 520 nm to 3.39 μm.[38] They

prepared a field-effect transistor using tellurium as a channel material to investigated its optoelectronic and electrical properties. The forbidden band of tellurium was studied by means of quantum molecular dynamics (QMD) simulations, which confirmed its applicability to mid-infrared (MIR) photodetectors. Under ambient conditions, the hole mobility of tellurium nanosheets reached up to 458 $cm^2V^{-1}s^{-1}$, and the peak external responsivity was 383 A/W (520 nm), 19.2 mA/W (1.55 μm) and 18.9 mA/W (3.39 μm) at different wavelengths, respectively. Due to the photogating effect, the high gains of up to 1.9×10^3 (520 nm) and 3.15×10^4 (3.39 μm) were obtained. Besides, the tellurium-based photodetector exhibited exceptionally high anisotropy at a communication wavelength of 1.55 μm, and a large bandwidth of 37 MHz was obtained due to the pure photoconductive effect.[38] Therefore, the device can cover the detection of short-wave infrared wavelengths and even the mid-infrared wavelengths. The FET tellurium-based photodetection was examined at the wavelengths of 520 nm, 1.55 μm, and 3.39 μm, respectively. As shown in Figure 6d-g, the dependence of the time response was first measured at the wavelength of 520 nm with source-drain bias (V_{ds}) = 1 V, and the polarization angles were spaced 15°apart. All photocurrent (I_{ph}) curves show an asymmetric peak at $V_g = 5$ V, which presents a threshold voltage shift about the channel trans-conductance (g_m), indicating a photogating effect of the photocurrent. A polar plot of the photocurrent dependence with respect to the polarization angle under the optimal conditions of $V_g = 5$ V and $V_{ds} = 1$ V has also been presented, with a dichroic color ratio of 1.9 at the 520 nm wavelength.

However, the detection range of the above tellurene-based devices is insufficient for better application in mid-infrared detection. Hence, a waveguide-integrated tellurene photodetector was proposed and designed (see Figure 6h).[82] After waveguide integration, the tellurene spectral range is extended to the mid-infrared at the wavelengths ranging from 2 to 3.6 μm, and the signal-to-noise ratio (SNR) is also improved. Figure 6i shows the minimum carrier concentration that is achievable in a graphene/$Ge_{23}Sb_7S_{70}$(20 nm)/tellurene metal-insulator-semiconductor (MIS) structure. In this MIS structure, a minimum carrier concentration of 7.5×10^{15} cm^{-3} can be obtained at a thickness of 10 nm for tellurene. The thicknesses lower than 10 nm are not desirable for photodetectors where an added bandgap would limit the spectral range of the detector. In addition to photodetectors, photomodulators and switches are the essential parts of photonic circuits, while tellurene is useful in photomodulator devices due to its high electro-optic (EO) activity. In mid-infrared integrated Puckers modulators, for example, tellurene is a semiconductor rather than an electrical insulator, which is fundamentally different from conventional EO crystals.[82] For this reason, the device behavior changes with the movement of free carriers given applied bias. Although strained silicon possesses similar properties, the free carriers in Si are heavily shielded in an insulator-semiconductor-insulator (ISI) configuration, thus resulting in a severely diminished Pockels effect. The 2D vdW materials on integrated photonic devices can be directly fabricated on chalcogenide glasses (ChGs) platforms and the amorphous compounds containing S, Te, or Se. Therefore, the ChGs on the telluride platform heralds a truly monolithic, wafer-level integration process for mid-infrared photonics that can be realized on standard substrates, which is an advancement that facilitates the scalable fabrication of mid-infrared optical systems.

3.2 $MoTe_2$ photodetector

As a compound of tellurium (Te) and molybdenum (Mo), $MoTe_2$ can be crystallized in 2D flakes and thinned into a single layer that is flexible and almost transparent. As a variety of TMDC material, it's also a semiconductor that can emit fluorescence. The bandgap of $MoTe_2$ varies from 0.83 eV in bulk to 1.1 eV in a monolayer, which is much smaller than that of other TMDCs such as WSe_2 and MoS_2. Also, the light absorption spectrum of $MoTe_2$ from visible light to near-infrared indicates its potential of use as a semiconductor in electronic or infrared detectors.

More and more 2D heterostructures are designed to achieve improved properties. The Fermi level and carrier density of 2D materials can be effectively adjusted through the gate bias in the heterostructures, which contributes a new solution to the making of tunable devices. However, the lack of well-designed relative band offset of the junction makes these 2D heterojunctions showing a quite limited ability to adjust the electrical and optoelectronic properties.[84, 85, 86, 87] While among these 2D heterostructures, the $MoTe_2$/BP heterostructure shows promising grid adjustable characteristics. By means of electrostatic gating, the $MoTe_2$/BP heterostructure can be adjusted to a *p*-*p* or *p*-*n* junction. Therefore, gate bias can be

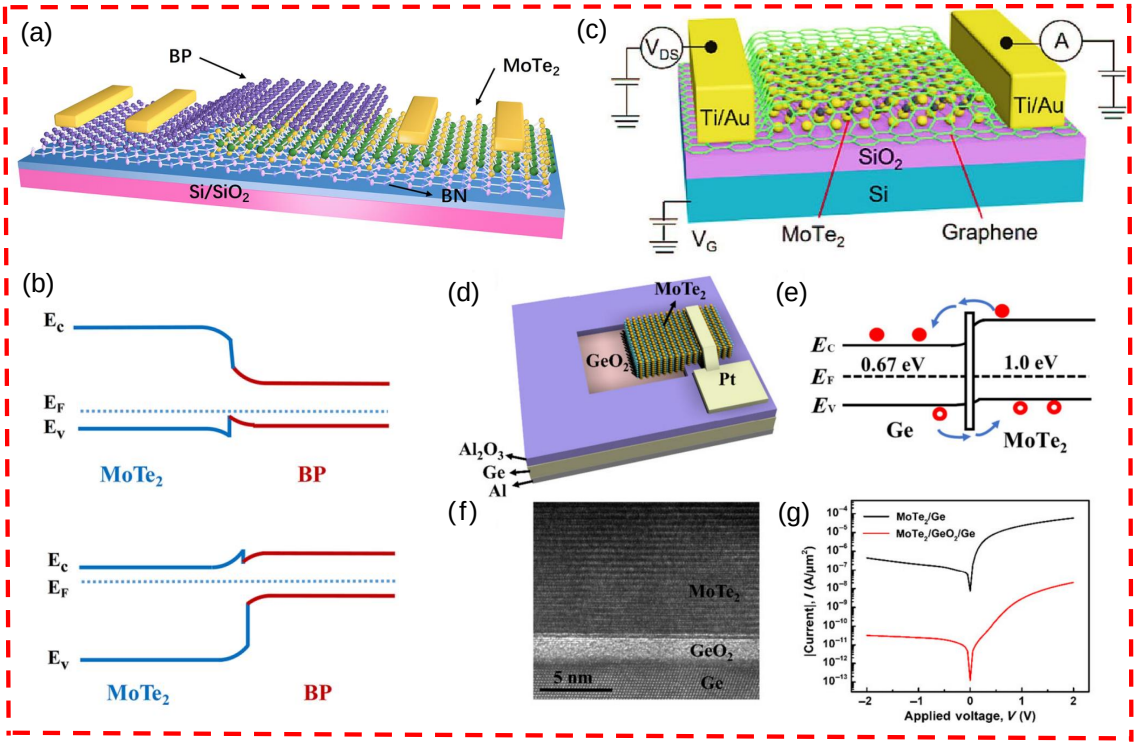

Figure 7: a) Schematic diagram of a $MoTe_2$/BP heterostructure device. b) Band alignment of $MoTe_2$-BP *p-p* (upper) and *p-n* (lower) heterojunction.[88] Copyright 2019, American Chemical Society. c) Schematic diagram of the $MoTe_2$/graphene phototransistor.[46] Copyright 2017, WILEY-VCH. d-f) Schematic diagram, energy band diagram and TEM images of the $MoTe_2/GeO_2$/Ge heterojunction. g) The I–V curves of the $MoTe_2$/Ge and $MoTe_2/GeO_2$/Ge heterojunction under dark.[89] Copyright 2019, Tsinghua University Press and Springer-Verlag GmbH Germany, part of Springer Nature.

effective in tuning the photovoltaic characteristics and direction of the rectification for the device. The grid tunable band alignment of $MoTe_2$ and BP explains this interesting phenomenon well. In addition, through the induction of the large inbuilt electric field formed between $MoTe_2$ and BP, this device shows excellent optical properties, including the fast response of external quantum efficiency and high responsivity.

As a group-IV semiconductor material with a bandgap of 0.67 eV,[90] Ge is considered to be a great material for the design of near-infrared photodetectors due to its small bandgap inducing a large absorption coefficient at near-infrared frequencies. In 2019, the $MoTe_2$/germanium (Ge) heterojunctions for photodetector applications were first investigated. Chen *et al.* systematically studied the optoelectronic properties of $MoTe_2$ and Ge heterojunction photodetectors under the context of 915 nm laser illumination.[89] Unexpectedly, $MoTe_2$/Ge heterojunctions photodetector showed excellent performance with a high responsivity of 12,460 A/W, a short response time of 5 ms, and a satisfactory specific detection rate of 3.3×10^{12} Jones.

Moreover, for reducing the reverse current in darkness, a GeO_2 layer was sandwiched by Ge and $MoTe_2$ (see **Figure 7**d). Surprisingly, it effectively reduced the current by more than four orders of magnitude. Actually, the GeO_2 layer acts as a thin barrier layer that reduces the hot carrier transport between Ge and $MoTe_2$, thus effectively suppressing the I_{leak} of the $MoTe_2$/Ge heterojunction.[89] The I-V curves of the $MoTe_2$/Ge and $MoTe_2/GeO_2$/Ge heterojunction in darkness are plotted in Figure 7g. The insertion of the GeO_2 layer reduces the I_{leak} to a very low level of 0.03 nA/μm^2. In addition, the GeO_2 layer also prevents carrier transport at the forward bias voltage, thus resulting in a reduction of the forward current in the dark. However, the more pronounced reduction in reverse current compared to forward current leads to an increase in rectification rate (133 without GeO_2 and 654 with it) when the insertion of the GeO_2 layer is followed. These results indicate that $MoTe_2$/Ge heterojunctions are applicable as a high-performance near-infrared photodetector in the future.

Additionally, the $MoTe_2$/graphene heterostructure photodetector has also been proven as fit for use in near-infrared light detection.[46] The device achieves a responsivity of about 970.82 AW^{-1} at 1064 nm and a broadband photodetection (visible-1064 nm). The electrons trapped in the local states of

$MoTe_2$ induce an effective light gating effect. The device exhibits an extremely high photoconductivity gain of 4.69×10^8 and a detection rate of 1.55×10^{11} $cmHz^{1/2}W^{-1}$. In addition, the device based on the $MoTe_2$/graphene heterostructure on the flexible substrate also shows high flexibility, which maintains an excellent photodetection ability (a high responsivity of about 60 A/W, at 1064 nm, V_{ds} = 1 V) through thousands of bending tests. Considering various merits like high responsiveness, broadband photodetection, and flexibility, $MoTe_2$/graphene photodetectors could be extremely suitable for application in bioimaging, wearable devices, and telecommunications.[46] It also offers new options for the development of flexible, low-cost, and efficient broadband NIR photodetectors.

3.3 $PdTe_2$ photodetector

The heterostructures formed by combining semiconductors with other materials address the drawbacks of previous deep ultraviolet (DUV) detectors, including low DUV/visible light rejection, small quantum efficiency, and fabrication difficulties. The weak van der Waals interactions between neighboring layers of 2D materials allow a variety of heterostructures to be used for high-performance photodetection. Characterized by type-II Dirac fermions and topological superconductivity, $PdTe_2$ has demonstrated consistent performance and high carrier mobility in tests.

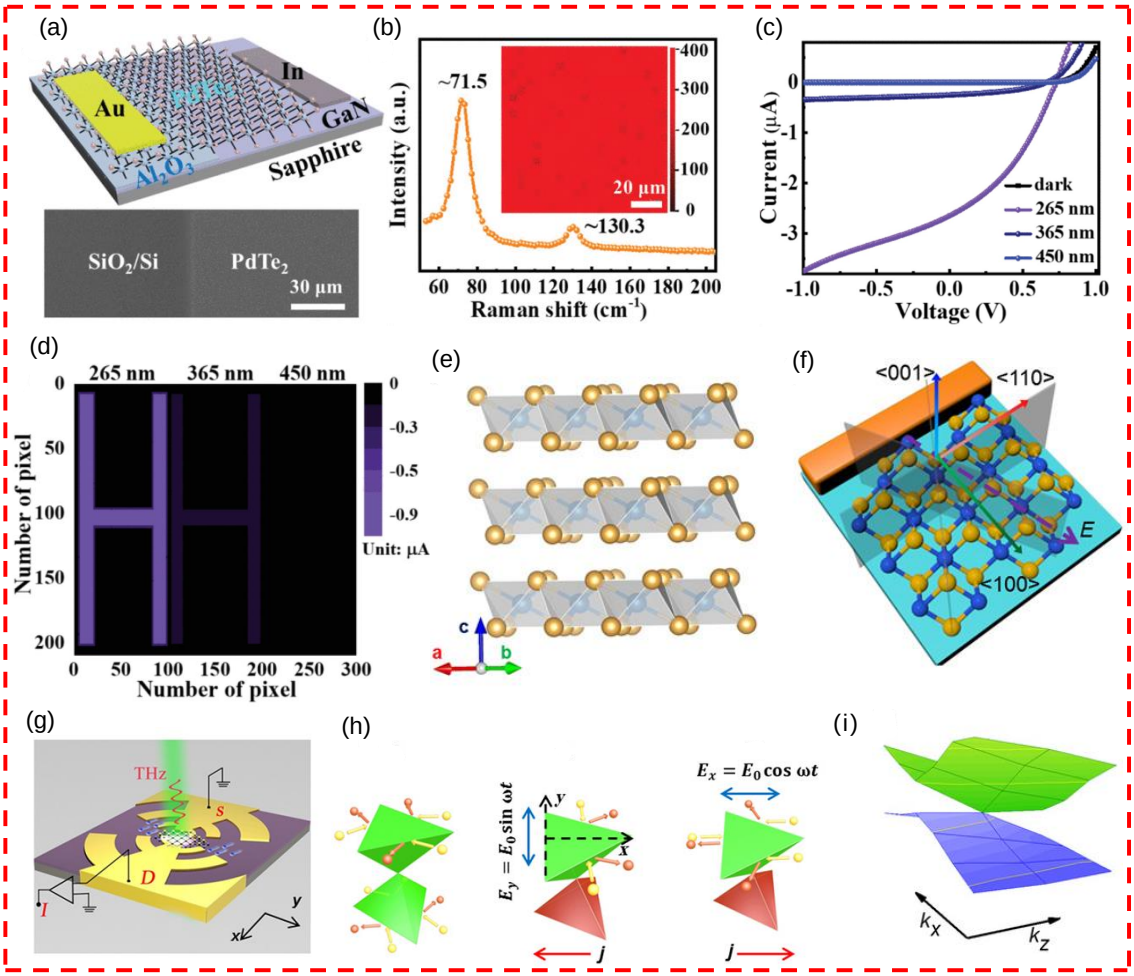

Figure 8: a) Schematic diagram of the $PdTe_2$/GaN photodetector (top panel) and the SEM image of multilayer $PdTe_2$ (bottom panel). b) Raman spectrum and 2D Raman mapping (inset) of multilayer $PdTe_2$. c,d) I–V curves (in dark) and the current contrast map under 265, 365 and 450 nm illuminations. [72] Copyright 2021, IEEE. e) Crystallographic structure of $PdTe_2$. f) Microscopic view of the metal-$PdTe_2$ contact along with the atomic chains. g) Schematic diagram of the $PdTe_2$-based photodetector. h) The PGE process and its polarization terahertz field dependence. i) The Dirac cone projection along the $k_x - k_z$ plane.[91] Copyright 2020, Guo *et al.*

The multilayer $PdTe_2$/GaN heterostructure with a Visible-Blind deep-UV photodetector device was

explored by combining the above features.[72] A multilayer large-area 2D $PdTe_2$ has been synthesized and transferred to GaN substrates for the formation of vertical heterostructures. A SEM image of the smooth surface of the multilayer $PdTe_2$ film is shown in **Figure 8**a. The Raman spectrum shows two peaks located at about 71.5 cm^{-1} (E_g) and 130.3 $cm^{-1}1$ (A_{1g}) (see Figure 8b). The high degree of continuity and homogeneity of the sample can be seen from the Raman spectrum. In the inset of Figure 8b, the peak intensity of the very narrowly distributed A_{1g} activity mode is displayed. Both the XRD image and the AFM image indicate that the synthesized $PdTe_2$ is a polycrystalline film consisting of submicron-sized crystal domains.[72] The I-V curves of the heterostructure show a satisfactory rectification ratio. In the meantime, the I-V curves under different wavelengths of illumination in the dark have also been drawn (see Figure 8c). The heterostructure shows the great response at 265 nm illumination, which is ∼10 times higher than that at 365 nm illumination. Besides, it shows poor sensitivity to the 450 nm illumination. In fact, the optical-image-sensing capability of $PdTe_2$/GaN heterostructure photodetector has also been explored. Light is illuminated through the hollow 'H' pattern and a shadow mask with a hollow square pattern is placed on top of it used to determine the effective area. A stepper motor was used to drive the photodetector to collect the current at each pixel point. Figure 8d shows the detected patterns under the 265, 365 and 450 nm illumination. It is clear that the image can be clearly identified under 265 nm illumination, the image under 365 nm illumination is faintly visible, and the image under 450 nm illumination is almost black. These results imply that the $PdTe_2$/GaN heterostructure DUV has great potential for optical image sensing applications. Moreover, such a pronounced photovoltaic effect at 265 nm illumination makes the heterostructure suitable for making a self-driven device. Beyond that, this device has a large photo-dark current ratio of 10^6 and shows outstanding photoresponse characteristics (peak ∼320 nm, cutoff ∼370 nm) in the DUV spectral region (220–360 nm). The DUV/visible (265 nm/450 nm) rejection ratio exceeds 10^4, evidencing its capability of visible-blind UV detection.

Furthermore, in the study of nonlinear optical response on topological semimetals (TSM), a photodetector based on type-II TSM $PdTe_2$ was developed.[91] $PdTe_2$ has a CdI_2-type structure and belongs to the $P\bar{3}m1$ space group, the crystal structure of which is illustrated in Figure 8e. In the absence of electric field applied, then three mirror planes exist on the surface of [001]. The spacing between the crystallographic planes can be obtained as 1.99Å[110]. The electron pocket near the Fermi surface in the k_x-k_y plane exhibits evident symmetry, which also indicates the inversion symmetry of $PdTe_2$ and the rotational symmetry around the c-axis. A schematic diagram of the device is shown in Figure 8g. Without any illumination, the flow of scattered electrons completely cancels out, while under illumination, a large number of carriers driven by the THz field generate a net shift current (See Figure 8h). Through an experimental investigation into the field polarization modulation of photgalvanic effect (PGE) in $PdTe_2$ and anisotropic photocurrents in $PdTe_2$ TSM, it is demonstrated that polarization-dependent photocurrent effects can produce directional photocurrents with high anisotropy. The excellent responsiveness (10 A/W), the fast response time (1s), and low noise equivalent power (NEP) (2 $pW/Hz^{0.5}$) at room temperature provide the basis for the fast imaging of macroscopic objects over large areas. The discovery is expected to promote the exploration into special optoelectronic phenomena.

3.4 $PtTe_2$ photodetector

As for topological semimetals, the peculiar band structure (such as type-II Dirac cone) of platinum telluride ($PtTe_2$) has been discovered in recent years. Due to the unique type-II Dirac fermions, $PtTe_2$ has become an intriguing candidate for optoelectronics. A CdI_2-type crystal structure [space group $P\bar{3}m1(164)$] of the bulk $PtTe_2$ is showed in **Figure 9**a,b.[73] Herein, vdW interactions maintain the fluctuating Te-Pt-Te atomic layers, thus making it a unique hexagonal structure. The distance between two neighboring layers is evaluated at approximately 0.522 nm.[92] Fast Fourier transform (FFT) and TEM images (see Figure 9c,d) also show a clear hexagonal lattice, while the lattice spacing of the (100) and (110) crystal planes are determined as 0.117 and 0.211 nm, respectively.[73]

The direct photocurrent generation in the terahertz (THz) band at low energy has been achieved in a planar metal-$PtTe_2$-metal structure at room temperature. Non-metallic materials are opaque and non-ionizing at infrared frequencies, but THz-band photons can penetrate most non-metallic materials and are

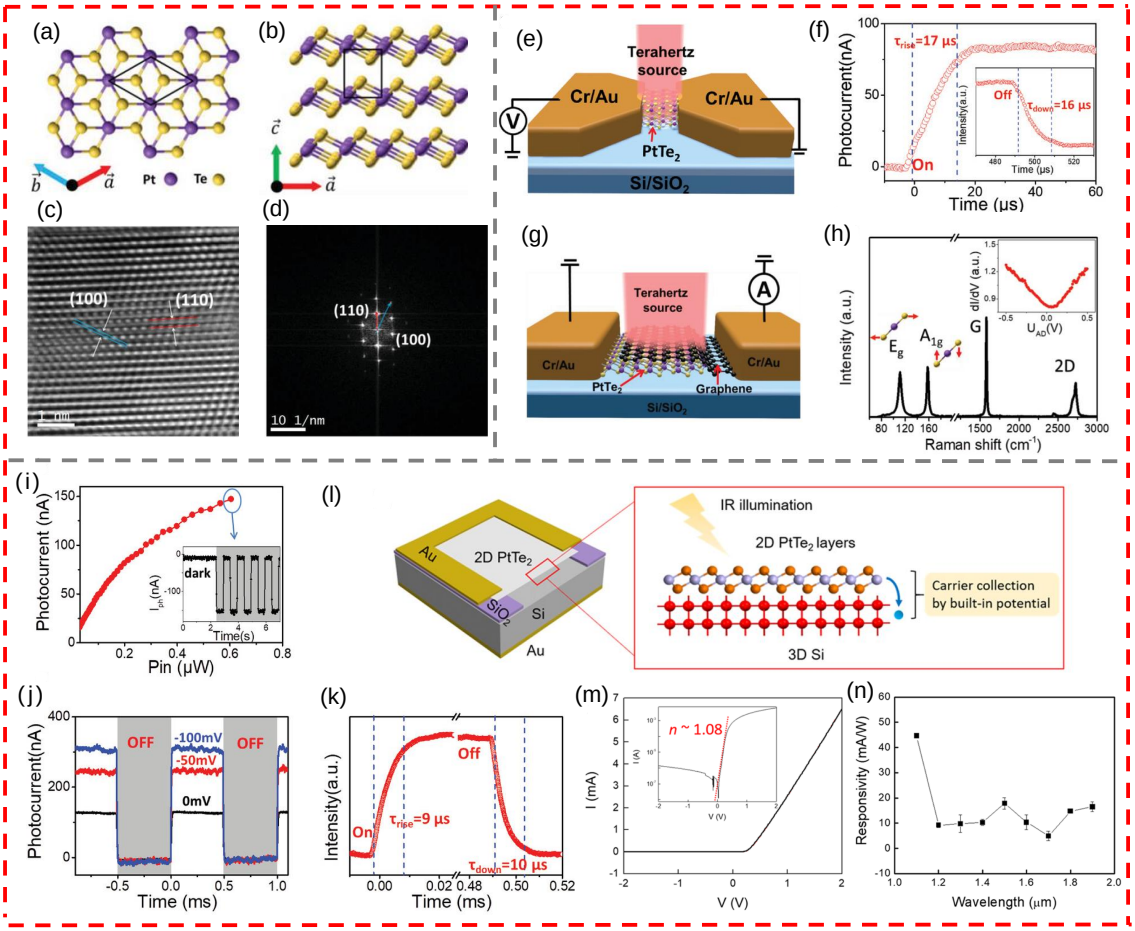

Figure 9: The top (a) and side (b) view of the $PtTe_2$ atomic structure. The TEM image (c) and FFT pattern (d) of the $PtTe_2$. e) Schematic diagram of $PtTe_2$-based THz detector. f) The rising edge and falling edge (the inset) of the photocurrent. g) Schematic diagram of graphene-$PtTe_2$ based THz detector. h) Raman spectrum of the $PtTe_2$-graphene heterostructure. i) The dependency of the photocurrent with respect to the incident power. j) Time response of the device at different bias voltages. k) The response/recovery times for the graphene-$PtTe_2$-based photodetectors under zero bias.[73] Copyright 2019, WILEY-VCH. l) Schematic diagram of $PtTe_2$/Si heterojunction device. m) I-V curve in darkness and the corresponding semi-log plot (inset). n) Illumination wavelength-dependent responsivity.[94] Copyright 2021, American Chemical Society.

commensurate with the characteristic frequencies of the rotational and vibrational spectra of biomedical molecules.[73] Thereupon, THz-band photons have a broad range of applications in (bio)medical, remote sensing, security, and nondestructive quality testing.[93] It has been demonstrated that gapless graphene FETs have the ability to perform detection in the region of overdamped plasma waves at room temperature. However, the low switching-off ratio greatly limits the performance of the device due to its gapless nature. $PtTe_2$ has been used in the planar detectors operating in the terahertz range. Figure 9e shows the schematic diagram of a THz photodetector based on $PtTe_2$ in contact with a bowtie type planar, where the bowtie type antenna is used to reinforce the THz electric field strength and also applied as an electrode. The device has a small resistance of 64 Ω, which is consistent with the semimetallic nature of $PtTe_2$. The pulse shape of the detector is well maintained at three bias voltages (0 mV, -50 mV, and -100 mV), with the response time and the recovery time being 17 and 16 μs, respectively. Also, the response is remarkably faster than typical thermal-based room-temperature detectors, which is fast enough for frame-rate imaging.

In order to better explore the proposed transportation properties of layered $PtTe_2$, multilayer graphene was prepared with $PtTe_2$ sheets stacked vertically to form a vdW heterostructure(see Figure 9g).[73] From the Raman spectrum shown in Figure 9h, it can be seen that, graphene and $PtTe_2$ retain their electronic properties at the vdW interface. Herein, two peaks at 111 cm^{-1} (E_g) and 157 cm^{-1}(A_{1g}) corresponds to $PtTe_2$, and the peaks at 1581 cm^{-1} (G) and 2726 cm^{-1} (2D) corresponds to graphene. The inset of Figure 9h shows the spectrum of the conductivity dI/dV exhibiting nonlinear characteristics especially at low

bias, which owing to interfacial tunneling between layers.[73] Meanwhile, due to the semimetallic nature of $PtTe_2$ and graphene, the resistance of the device drops from 1.2 kΩ to 600 Ω at higher bias voltages, which is less than the resistance of typical semiconductor heterostructures by a factor of at least 100. Afterwards, the $PtTe_2$/graphene heterojunction device was further explored as a photodetector. At zero or negative bias, the interfacial carrier diffusion process of $PtTe_2$ and graphene is non-equilibrium. Figure 9i shows the photocurrent curves of the graphene-$PdTe_2$ heterostructured device as measured at different incident powers and without applied bias. The photocurrent saturates at 0.6 μW, which is different from the result of the original device, demonstrating the capability of low-power detection and high-efficiency interlayer coupling that the heterojunction device has. Figure 9j,k shows the response speed of the heterostructured device under fast modulated radiation at 1 kHz. Even though the graphene-$PtTe_2$ device is much more resistive than the original one, its pulse shape is well maintained and it has a good signal-to-noise ratio and fast response time (∼10 μs). This is a significant advantage over commercially available Schottky diode detectors.

Besides, $PtTe_2$ contributes new ideas to mid-infrared (MIR) photodetection. First of all, $PtTe_2$ thin films exhibit typical semimetallic behavior, which is consistent with the calculation results of DFT.[92] Secondly, the combined multilayer $PtTe_2$ and Si results in the formation of $PtTe_2$/Si heterojunctions with satisfactory outcome of rectification effect.[94] The 2D $PtTe_2$ layer consists of single crystal domains with highly preferred [001] orientation along the normal direction, which reduces the impact of interfacial defects and ensures effective out-of-plane carrier transport. For instance, the vdW bonded $PtTe_2$ layers coupled with 3D covalently bonded Si wafers were explored for a novel broadband MIR photodetector. Although the 2D $PtTe_2$ layer and the Si wafer are less sensitive to MIR, it is observed that 2D $PtTe_2$/Si heterojunctions exhibit a large number of photoexcited carriers under MIR illumination in the spectral range of 1–7 μm. Its superior physical properties can be attributed to the Schottky junction properties. Figure 9l shows a schematic diagram of a 2D $PtTe_2$/Si MIR photodetector. Due to its Schottky properties, a strong built-in potential is applied. The presence of this intrinsic Schottky junction facilitates the efficient separation and collection of photocarriers, thus improving the mid-infrared responsiveness of the structure. Additionally, the variation in optical transmittance and conductivity of the 2D $PtTe_2$ layer has been investigated, and the result of which is that the optical transmittance of the device decreases and the electrical conductivity increases as the thickness of the platinum seed increases. Figure 9m selects a two-terminal current-voltage (I-V) curve, which was obtained from a representative device prepared from platinum with a 4.5 nm thickness. Due to the interfacial Schottky junction between the metallic 2D $PtTe_2$ layer and the semiconductor Si, a highly asymmetric I-V characteristic is observed in the dark, along with a high rectification ratio at ±2 V. The inset shows the corresponding semi-logarithmic plot. Figure 9n shows the response rate versus illumination wavelength in the NIR range of 1.1–1.9 μm. Probably due to a significant decrease in the absorption of silicon, the responsivity initially decreases after 1.1 μm and then becomes almost saturated beyond that wavelength. However, the observed responsivity in a similar wavelength range is still significantly greater than the values as measured with a separate 2D $PtTe_2$ layer. Meanwhile, a wafer-scale 2D $PtTe_2$ was prepared by taking a simple tellurium vapor transformation approach,[47] which resolves the downsides like strict operational requirements, environmental toxicity, and the high cost of the materials dominated by conventional InSb, HgCdTe alloys, and quantum superlattices. Also, it breaks various limitations including the poor stability of BP-based MIR photodetectors and the difficulties in large-area integration, which enables $PtTe_2$ to show its superiority in such settings as civil and military surveillance and night vision.

3.5 WTe_2 photodetector

WTe_2 is a unique material in the family of TMDCs, which has been proposed as an example of type-II Weyl semimetals. Monolayer WTe_2 shows anisotropic atomic figuration and basic features, which makes it distinguishable from the semblable monolayer crystals of TMDCs, such as $MoTe_2$, $MoSe_2$, WS_2, WSe_2, and MoS_2. The previous DFT calculations show that WTe_2 has T_d and H phase (see Figure 10 (a) and (b)).[95] Herein, H-WTe_2 (4.54 eV/atom) has lower cohesive energy than T_d-WTe_2 (4.57 eV/atom) and the unit energy of T_d-WTe_2 is about 0.075 eV lower than H-WTe_2. Therefore, the monolayer T_d-WTe_2 shows

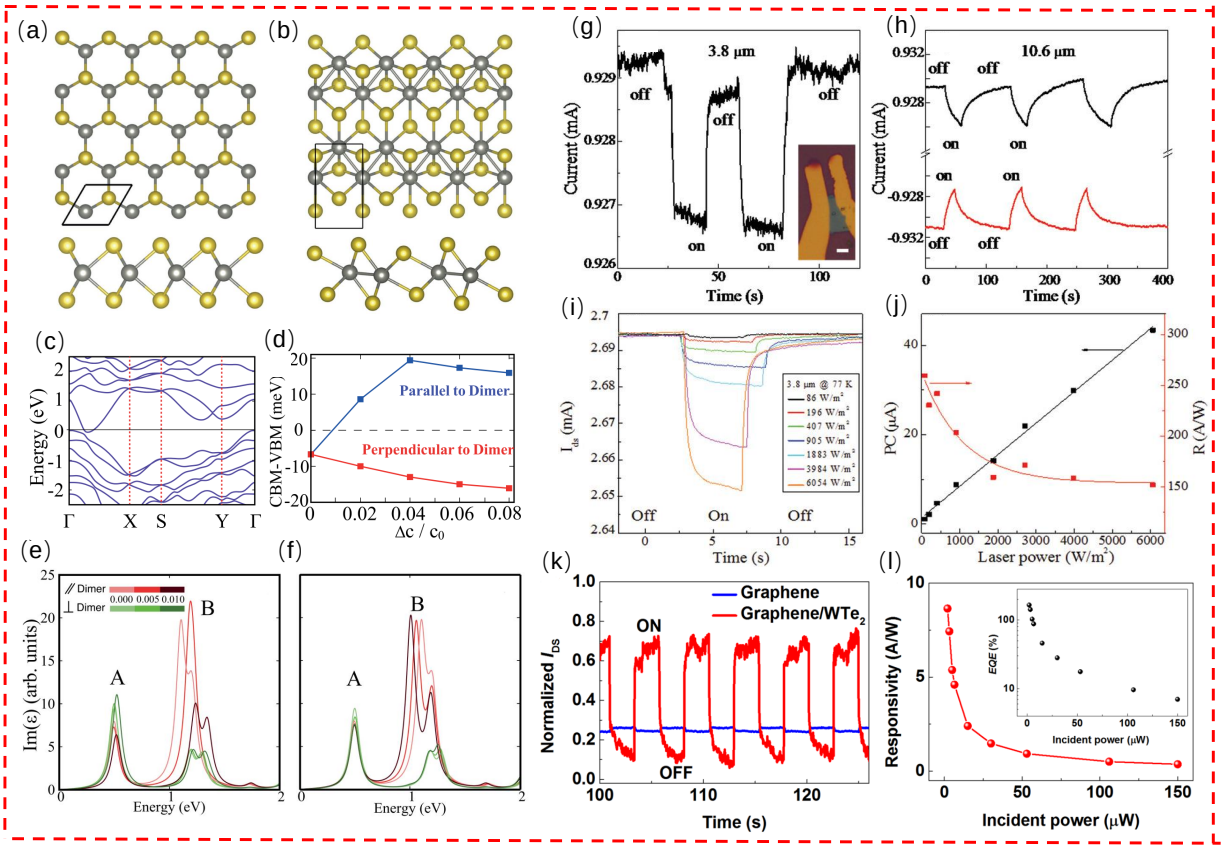

Figure 10: a,b) H phase (a) and T_d phase structure of monolayer WTe_2. c) Electronic bandstructure of monolayer T_d-WTe_2. d) The energy difference between CBM and VBM of T_d-WTe_2 under strain. e,f) Strain-dependent imaginary part of the dielectric function of monolayer T_d-WTe_2 when strain is along (e) and perpendicular (f) to W-W dimers.[95] Copyright 2016, AIP Publishing LLC. g,h) Anomalous photoresponse of a WTe_2 nanoflake under laser irradiation. (g) 3.8 μm, $V_{ds} = 0.1$ V. (h) 10.6 μm with $V_{ds} = \pm$ 0.1 V. i) WTe_2 photoresponses to 3.8 μm laser under different power. j) Photocurrent values and photoresponsivity from (i).[43] Copyright 2018, WILEY-VCH. k) Time-resolved photoresponse of pure graphene device and graphene/WTe_2 heterostructure device. l,m) Responsivity and EQE of the graphene/WTe_2-based transistor as function of the incident light power.[96] Copyright 2018, Liu *et al.*

greater stability. Moreover, anisotropy in both Poisson's ratio (ν) and in-plane stiffness along x (parallel to dimer) and y (perpendicular to dimer) directions of the T_d-WTe_2 monolayer has also been revealed. The in-plane stiffnesses as calculated for the dimer along the x and y directions is 4.45 eV/Å^2 and 6.56 eV/Å^2 respectively. They are both much lower than those for graphene (21.42 eV/Å^2) and functionalised graphene-like materials, suggesting that WTe_2 has better flexibility than these materials. Hence, the better flexibility will make T_d-WTe_2 extensively applicable in wearable devices.

The energy bandstructure of the monolayer T_d-WTe_2 is presented in Figure 10c. T_d-WTe_2 shows a semimetallic ground state when it is not strained, and the CBM is 6.7 meV lower than the VBM.[95] The conduction band traverses the Fermi energy level along the Γ-X direction, *i.e.*, the W-W dimer direction, which also implies that the occurrence of dimerization makes some contributions to the metallic ground state of the T_d-WTe_2 monolayer. Also, the strains in different directions affect the energy band structure of T_d-WTe_2 to different degrees (see Figure 10d). As the tensile strain is employed parallel to the W-W direction, the CBM surges and the VBM drops. Finally, the WTe_2 undergoes the transition from semimetal to semiconductor when the 1% strain is applied to it. When the strain along y direction is used, the compound always maintains the semimetallic state. Moreover, the dielectric function of T_d-WTe_2 changes differently when external strain is applied to it in different directions. As shown in Figure 10e,f, in the absence of strain, the location of B-peak is slightly different along different various directions. While a tensile strain is used along the dimer, the B-peak shifts towards the higher energy. Besides, the peak dielectric function along the dimer-parallel direction occupies the same position in the perpendicular direction. In contrast, when the strain is applied perpendicular to the dimer direction, the B-peak shifts

to lower energy. Besides, when the strain rises to 0.010, the peaks of the dielectric function along and perpendicular to the dimer direction are split. Meanwhile, the dielectric function along y direction is irrelevant to the adopted strain and its peak is not converted as the external strain changes.

As a type-II Weyl semimetal, to a certain extent, the 2D crystal and electron anisotropy properties of T_d-WTe_2 facilitate the subtle detection of long-wavelength polarized light. It has been demonstrated that T_d-WTe_2 has a significantly anomalous photoresponse in the visible to the far-infrared band, as shown in Figure 10g,h.[43] Meanwhile, its responsiveness is enhanced with the decreases in temperature, and the photocurrent and responsivity of WTe_2 can be further increased to 40 μA and 250 A/W at the liquid nitrogen temperature, with the signal-to-noise ratio reaching up to 500. This can be attributable to some extent to the PTE effect. In addition, the photocurrent of WTe_2 is polarization sensitive, with the maximum laser polarization parallel to the zigzag direction and the minimum laser polarization along the armchair direction with a ratio up to 4.9. It indicates that the anisotropic tunability possessed by the electronic structure of WTe_2 under polarized light, which matches its crystal structure. It is also suggested that the irradiation with a linear polarization light is an efficient solution to adjusting the electronic structure of the WTe_2 surface. Large anomalous anisotropic photocurrents can be induced, demonstrating the advantage of WTe_2 in the design of infrared photodetectors at room temperature.

For WTe_2, each chiral Weyl node can have an impact on the motion of electrons directly and shows a unique topological enhancement effect in the aspect of photoresponse. In addition, it was demonstrated through experimentation that the WTe_2 films with hyperbolic plasma surfaces have a strong capability of visible and far-infrared (16–23 μm) absorption capabilities. Nevertheless, pure WTe_2 possesses high conductivity carrier density (10^{19} cm-3) and carrier mobility ($\sim$1000 $cm^2V^{-1}s^{-1}$), which implies that large dark current and high power expense are adverse to widespread manufacture and further development for this kind of photodetector. Therefore, to design 2D heterojunctions is a way to reduce the total power consumption by semimetals in the dark. As one of the typical examples, the WTe_2/MoS_2 van der Waals heterojunction is examined to verify its optical properties for future use in the field of photodetection.[97] The dark current in it is always less than 1 nA at 1 V, which can help reduce power consumption by the semimetallic detector. The photoresponse characteristics of this heterojunction are dependent on the wavelength of the light. The optical responsivity R, EQE, and the photodetection rate D^* can reach up to 31.1 A/W, 9640% and 4.36×10^{10} Jones at 400 nm, respectively (while 0.18 A/W, 21%, and 2.5×10^8 at 1050 nm). It is thus clear that the device shows secondary and stable photoresponsiveness and exhibits a slow response when the wavelength of light ranges between 400 and 500 nm, while the photoresponse is smaller and swifter as the wavelength of radiation exceeds 700 nm. In addition, the 2D heterojunction shows a tunable photoresponse closely related to the thickness of WTe_2, and the positive anomalous photoresponse is closely associated with the thickness of WTe_2. The threshold thickness ranges between 10.7–27.8 nm. When the thickness of WTe_2 decreases to 6.8 nm, an anomalous optical response occurs. Therefore, it can be concluded that the 2D Schottky junctions based on WTe_2/MoS_2 shorten a lot of dark currents and extra noise, which not only makes power consumption low in detecting infrared light but also helps achieve high sensitivity to low illumination.[97] The great potential of topological half-metal van der Waals heterojunction photodetectors such as WTe_2 was demonstrated.

Finally, the study of the all-semimetal 2D heterostructure also plays an irreplaceable role in guiding the development of photodetector. The detector based on the WTe_2/graphene heterostructure is representative of these devices.[96] As shown in Figure 10k, the WTe_2/graphene device maintains a long-period stable current after experiencing the periodic current excitation. Also, the device produces a better performance than the pure graphene device since it exhibits a stronger current. As is shown in Figure 10l, R and EQE are both non-linear and rise up as the illumination power diminishes. It can be seen that the maximum of R is $\sim$8.7 A/W, which is based on the radiation of low incident energy of 2 μm with the V_{ds}= 0.5 V. In the same situation, the corresponding EQE is calculated to be 165%, which far exceeds a lot than that of the monolayer graphene detector. The main reason for the enhancement of the current is that the interfacial effect can easily separate the electron-hole pairs owing to the photothermoelectric and photovoltaic effects.

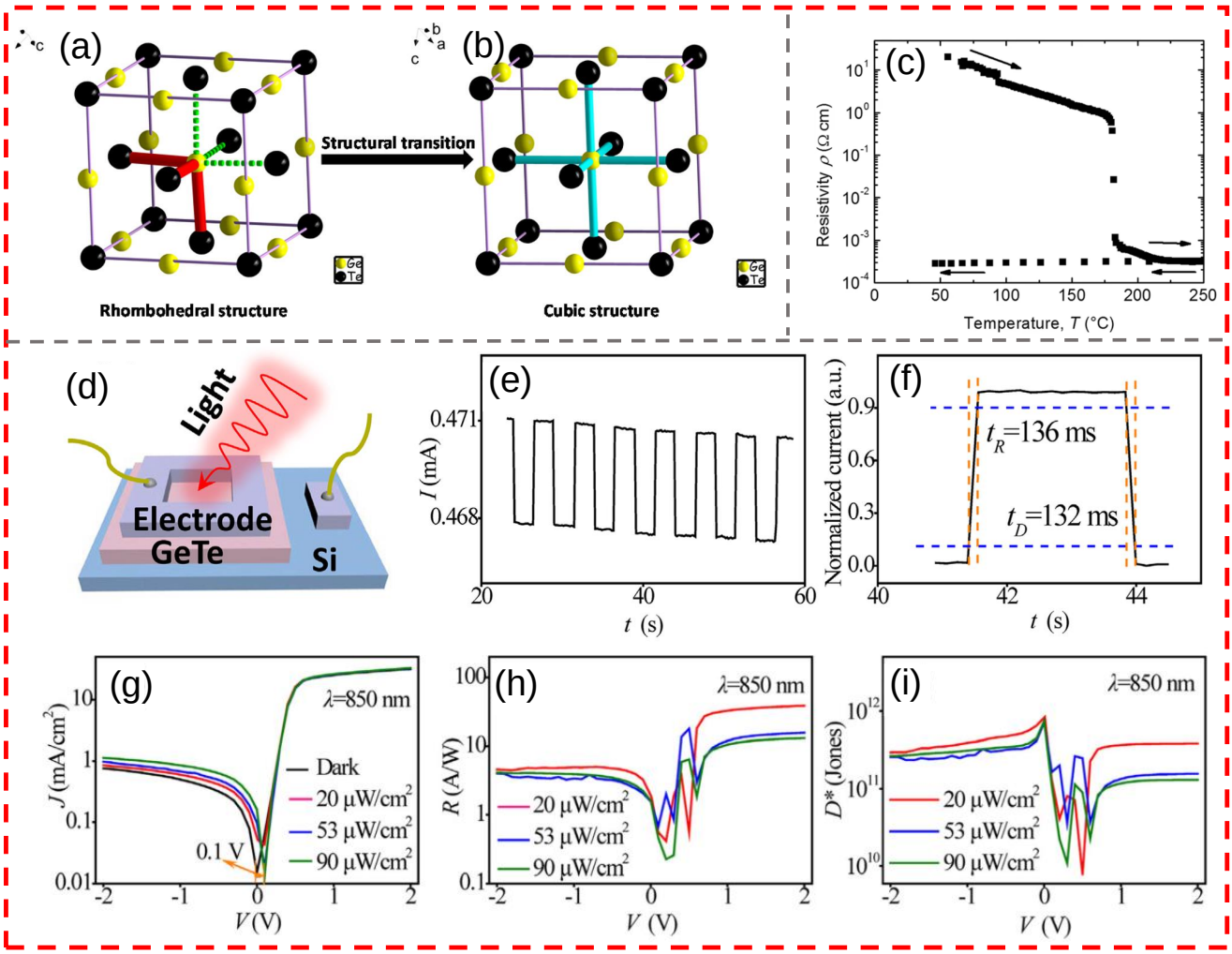

Figure 11: a,b) The rhombohedral (a) and cubic (b) structure of GeTe. [100] Copyright 2018, American Chemical Society. c) Resistivity of GeTe film as a function of temperature.[101] Copyright 2017, Mantovan *et al.* d) The structure of p-GeTe/n-Si heterojunction photodetector. e,f) Temporal photoresponse of the device. g-i) The $log(J) - V$, $R - V$, and $D^* - V$ curves of the GeTe/Si heterojunction photodetector, respectively.[102] Copyright 2020, Zhao *et al.*

3.6 GeTe photodetector

As a group-IV semiconductor material with a narrow bandgap, germanium telluride (GeTe) is a phase-changing material (PCM) that exhibits a reversible transition between crystalline (SET) and amorphous (RESET) with the assistance of electrical/optical pulse. It has been commonly applied in the settings of thermoelectricity, phase change storage and switch.[98, 99] At the same time, due to its excellent photoelectric properties, it also has a relatively broad space of development in the field of photoelectric detection. **Figure 11**a,b shows the two structures of the GeTe crystal, namely rhombohedral structure, and cubic structure.[100] The difference is that in the cubic structure, the germanium atom is located in the center of the octahedron as formed by the Te atom. In the rhombohedral structure, the germanium atom deviates from the center of the octahedron. In terms of symmetry, the rhombohedral structure is an asymmetric octahedron, consisting of three longer bonds (green dashed line) and three shorter bonds (red line). In contrast, the cubic structure shows symmetry and all Ge-Te bond lengths are equal.

As a narrow bandgap semiconductor, GeTe possesses excellent electrical properties. The resistivity of PCM plays a vital role in the efficiency and stability of the material. From Figure 11c, it can be found out that as the temperature increases, the resistivity declines in the liquid condition but rises in the solid condition, indicating that GeTe has the characteristics of liquid semiconductor.[101] At the same time, a significant change in resistivity can be observed at around 180°, which is obvious, and this is a transition from the amorphous phase to the crystalline phase. It can be seen that the resistivity of the crystalline

phase of GeTe is relatively low, while that of the amorphous phase is relatively high. Besides, the bandgap energy (E_g) can also be significantly affected by the phase change. The E_g of GeTe film before and after annealing correspond to 0.85 eV and 0.77 eV, respectively.[103] Hence, the crystalline state has a lower bandgap energy E_g than the amorphous state which can be attributed to the long-range order of the crystalline GeTe lattice.

The optical properties shown by different phases of GeTe are also different. Recently, Zhao *et al.* conducted experiments to analyze the ultraviolet-visible-near-infrared (UV-Vis-NIR) absorption spectroscopy of the GeTe film during a study on the properties of the GeTe film before annealing (amorphous state) and after annealing (crystalline state).[103] There is an absorption peak at 610 nm after annealing, indicating that the absorption coefficient of the annealed GeTe film is much higher than that of the unannealed GeTe film. That is to say, the absorption coefficient of crystalline GeTe is far higher than that of amorphous. Additionally, in the range of infrared light, the absorption coefficient will decrease as the wavelength increases. In addition, the refractive index of the amorphous GeTe state is lower because it is formed by covalent bonds, while the refractive index of the crystalline state is higher due to the higher polarizability of the *p*-orbital resonance bond.

A photodetector comprised of crystalline GeTe and Al has also been proposed to conduct a specific study on the optical properties of GeTe. The log(J)-V characteristics of the device under darkness or irradiation show that the current density increases significantly when there is light, and the ratio of photocurrent to dark current is very high, evidencing the excellent photoresponse characteristics. In addition, responsivity (R) and detectivity (D^*) are two non-negligible values for the characteristics of light response characteristics. As the bias voltage exceeds 0.5 V, the value of R ranges between 88 and 650 A/W, while the value of D^* ranges between 2×10^{13} and 6×10^{14} Jones (1 Jones = 1 cm $Hz^{1/2}$ W^{-1}). Moreover, in the infrared band, both R and EQE have higher levels and decline as the wavelength increases. In contrast, owing to the amorphous characteristics of the unannealed GeTe film, the unannealed device shows no photoresponse. Thereupon, the crystalline GeTe has a great potential of development in respect of infrared detection.

Apart from that, but GeTe has also been better applied in the manufacture of heterojunction photodetectors. The GeTe/Si heterojunction photodetector has a relatively stable response current while the rise time ($t_R = 136ms$) and fall time ($t_D = 132ms$) are almost symmetrical (see Figure 11f). In order to better understand the light response characteristics of this GeTe/Si-based detector, the $log(J) - V$, $R - V$, and $D^* - V$ curves were placed in Figure 11g,h,i, respectively. The voltage corresponding to the minimum values of the photocurrent and dark current density are different by 0.1 V. Also, the R and D^* are 6–15 A/W and 1–8×10^{11} Jones, repectively. In general, the GeTe/Si heterojunction shows relatively good photoelectric response characteristics at room temperature, which may result from the narrower direct bandgap and higher absorption coefficient of crystalline GeTe.

3.7 SnTe photodetector

Topological crystal insulators (TCIs) have been considered as suitable for use in ultra-broadband photodetectors in the UV to THz range due to their gapless surface states and narrow bandgaps of bulk. However, the low response of photodetectors based on TCIs has restricted their further applications. However, the related photodetector of SnTe, which is also a variety of TCL material, exhibits high responsiveness and ultra-wide spectral response. Meanwhile, the heterostructured photodetectors of SnTe and Bi_2Se_3 or Si are capable of self-driven operation and exhibit a broad-spectrum high-frequency response to near-infrared light.[104]

As revealed by first-principles calculations, the bulk SnTe retains a similar strain-dependent bandstructure to that of tellurene materials.[44] Figure 12e shows the changes in bandstructure with the strain, as well as the contribution made by the *s* and *p* orbitals of Te to the corresponding electronic states (indicated by the size of dots). As the strain increases, the bandgap starts to decrease and then increases again. When the strain exceeds 3%, the energy band inversion disappears, *i.e.*, the Te-*p* orbitals shift from the conduction band edge to the valence band edge. In contrast, the strain-induced change in energy band for SnTe nanofilms exhibits a distinct even-odd oscillation owing to its two-fold screw rotation along the

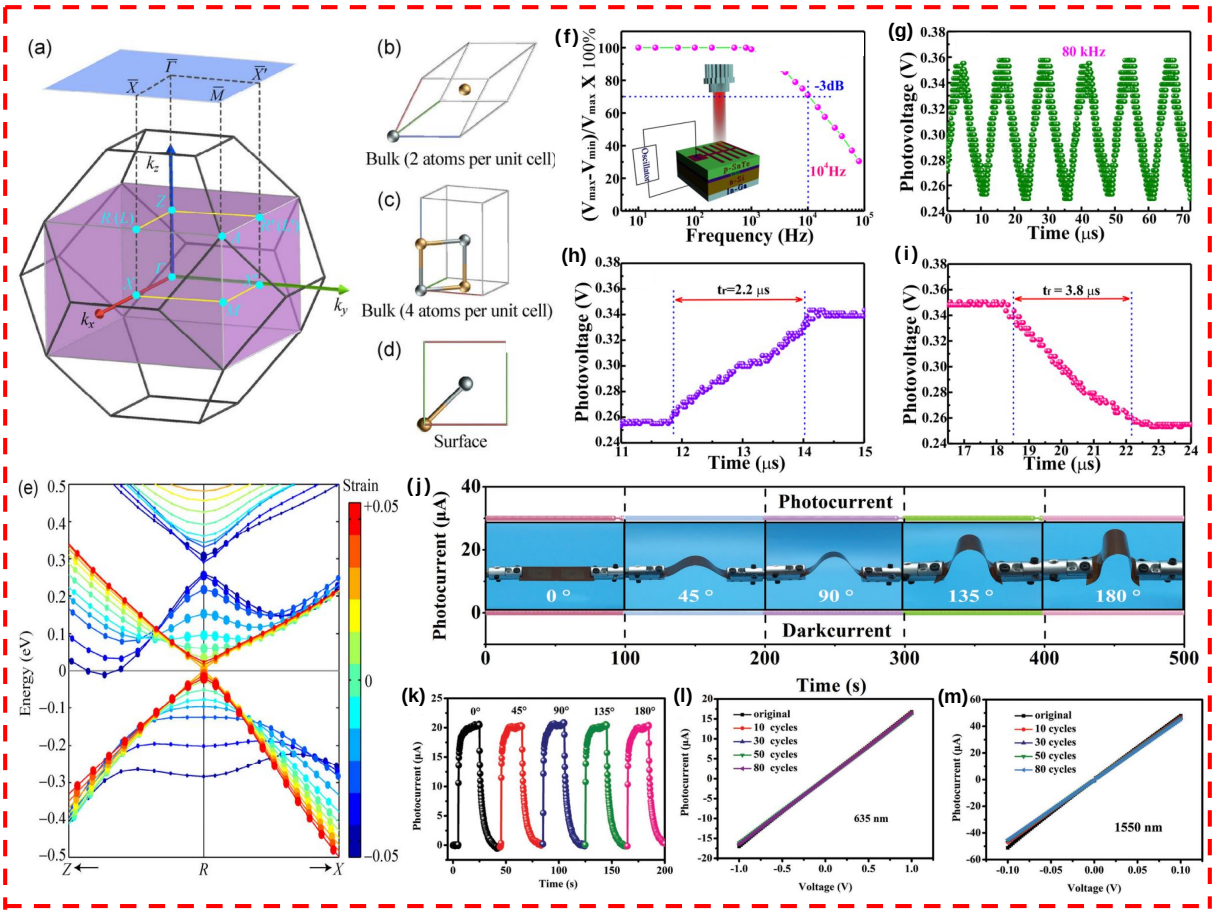

Figure 12: a) Brillouin zones for bulk (the black and purple are for two/four atoms per unit, *i.e.* b),c) respectively) and SnTe membrane (the blue one) in different unit cells. Te: yellow atoms; Sn: gray atoms. e) Strain-dependent electronic bandstructure of SnTe.[44] Copyright 2014, Tsinghua University Press and Springer-Verlag Berlin Heidelberg. f) Relative balance $(V_{max} - V_{min})/V_{max} \times 100\%$ vs frequency of pulsed light plot. g) Instantaneous open-circuit voltage (V) response of the photodetector (with pulsed frequency of 80 kHz and 980 nm light irradiation). h,i) Characteristic response times of the photodetector at rising (h) and falling (i) edge.[105] Copyright 2017, American Chemical Society. j) Photocurrent and dark current are evaluated for SnTe photodetectors under 1550 nm illumination at various bending radii (from 0 to 180 °). k) Time-dependent photocurrent for different bending radii. l,m) Under 635 nm (l) and 1550 nm (m) laser illumination, the photocurrent is a source-drain bias function with different bending cycles varying from 0°to 90°.[106] Copyright 2018, WILEY-VCH.

[010] and [110] directions. Besides, it is only retained in the even-layered symmetrical SnTe nanofilms. Nevertheless, the energy band of the 2D SnTe material is always maintained at 0–0.15 eV, and such a low bandgap allows it to respond well to NIR spectroscopy. The high-quality SnTe nanosheet photodetectors grown directly on the Si surface through physical vapor deposition (PVD) showed excellent photoresponse and periodic photocurrent similarity for a broad spectrum from 254 nm to 4650 nm in the experiments. Under the laser irradiation of 635 nm and 1550 nm, the photocurrent shows an excellent linear increase with the rise in optical power until the optical power saturates the photocurrent. Notably, SnTe is also capable of forming flexible photodetectors on PET substrates. Under the light irradiation of 635 nm and 1550 nm, the photocurrent and dark current of the flexible photodetectors remain basically despite the bending from 0 to 180 degrees, while the photocurrent curves of the devices under bending are essentially unchanged, with a good linearity shown under light irradiation at both wavelengths.

Heterojunction detectors are extensively used in the field of optoelectronics. As mentioned earlier, the materials with common properties on their own combined together are likely to have good optoelectronic properties, for which they can be used to fabricate 2D material photodetectors with an excellent performance in detection. Among the SnTe heterojunction photodetectors, the SnTe/Si vertical heterojunction detector is an outstanding one.[105] Unlike the Si-based detector, SnTe/Si heterojunction photodetectors

use the different positions of the electrodes to allow SnTe/Si to form *p-n* junctions. In the experiment, the laser irradiation of 1064 nm, 1310 nm and 1550 nm was employed respectively, with all exhibiting tens of cycles within the highly-similar photocurrent profiles as well as the photocurrent magnitudes as modulated by optical power. In the further experiments with high frequency light irradiation, the performance of the device in high photocurrent response was fully demonstrated, the results of which showed that the SnTe/Si heterojunction detector was able to respond to high-frequency light signals with the frequencies up to 10^5 Hz and an intrinsic response bandwidth of 10^4 Hz, which is attributed to the helical nature of the SnTe films surface state that suppressed electron backscattering and achieved excellent transmission with high carrier mobility.

Further studies have shown that the photoresponse exhibits long-term stability and repeatability under the light irradiation with a 80 kHz frequency, while the time taken for photocurrent to rise and fall reaches 2.2 μs and 3.8 μs, respectively, both of which are much faster than those of SnTe photodetectors (0.21 s and 0.73 s).[105] Similar to the aforementioned SnTe photodetectors, SnTe/Bi_2Se_3 heterojunction photodetectors as fabricated by PVD also possess the capability of self-powered operation and can achieve excellent photoresponse performance and high response speed under the context of self-powered operation.[104] The device shows a continuous increase in photocurrent with light intensity throughout the voltage region in the presence of reverse bias voltage, with good linearity and higher sensitivity to IR light can be observed. In addition, the 1550 nm pulsed light irradiation data suggested that the devices exhibited similar photoresponse images over several cycles at both reverse bias voltage of 3 V and zero bias voltage, which demonstrates that the SnTe/Bi_2Se_3 heterojunction photodetector is able to operate consistently whether under zero or reverse bias. Also, the modulation amplitude of the reversible photocurrent turn-on light intensity became more significant with reverse bias voltage. The repetitive response curve to high frequency light further highlights the excellent performance of the device. In the experiments, the signal pulses were measured at the optical frequencies of 100 Hz, 1 kHz, and 20 kHz, respectively. Moreover, SnTe/Bi_2Se_3 showed ultra-high response properties, with the optical response pulses rising and falling at 6.9 and 19.2 μs, which indicates its excellent performance in photodetection.

3.8 GaTe photodetector

As a highly stable tellurium metal in a dry environment at room temperature, GaTe is extensively used in the optoelectronic and semiconductor industries and so on.[107, 108, 109, 110, 111, 112] The structure of GaTe is diverse, with the material appearing as a monoclinic phase in the bulk state, and it has a hexagonal phase when the layers are reduced to a few or even only one. The monoclinic phase of GaTe appears as a semiconductor with a direct bandgap of 1.7 eV, while the hexagonal phase of GaTe appears as an indirect bandgap, with the VBM shifting towards the Γ point as the number of layers rises and rapidly approaching the energy bandstructure of bulk GaTe.[113] However, the special position of the VBM may provide an opportunity for optical charge to jump at the local CBM, thus making the hexagonal phase GaTe a promising application in photodetection. Unfortunately, we have not found any photodetector applications in photodetector for hexagonal phase GaTe. Most of the existing photodetectors made out of GaTe are based on GaTe heterojunctions. The advantages of them can be summarised as follows. Firstly, GaTe-based flexible detectors demonstrate high bending durability and high stability, which opens up many scenarios of applications for wearable photodetectors. Secondly, some heterojunction photodetectors have a high sensing current switching ratio, which makes it advantageous over many other 2D material photodetectors. Lastly, some of the heterojunction photodetectors can operate at the unbiased voltage and perform better in zero-bias operation than most zero-bias photodetectors.

In recent years, GaTe nanowires-based photodetectors have also attracted some attention. Both the GaTe nanowire and nanosheet can be grafted onto polyethylene terephthalate (PET) substrate to generate flexible photodetectors.[116, 114] However, whether it is surface charge activity or sensing response area, 1D GaTe nanowires are inferior to 2D GaTe nanosheets. GaTe nanosheet photodetectors show significant photoresponsive properties for all wavelengths from ultraviolet (UV) to visible, but it can also be found out that GaTe nanosheet detectors are susceptible to environmental and surface adsorption effects. It can be seen from the **Figure 13**b that the dark and photocurrents shift to higher current levels during

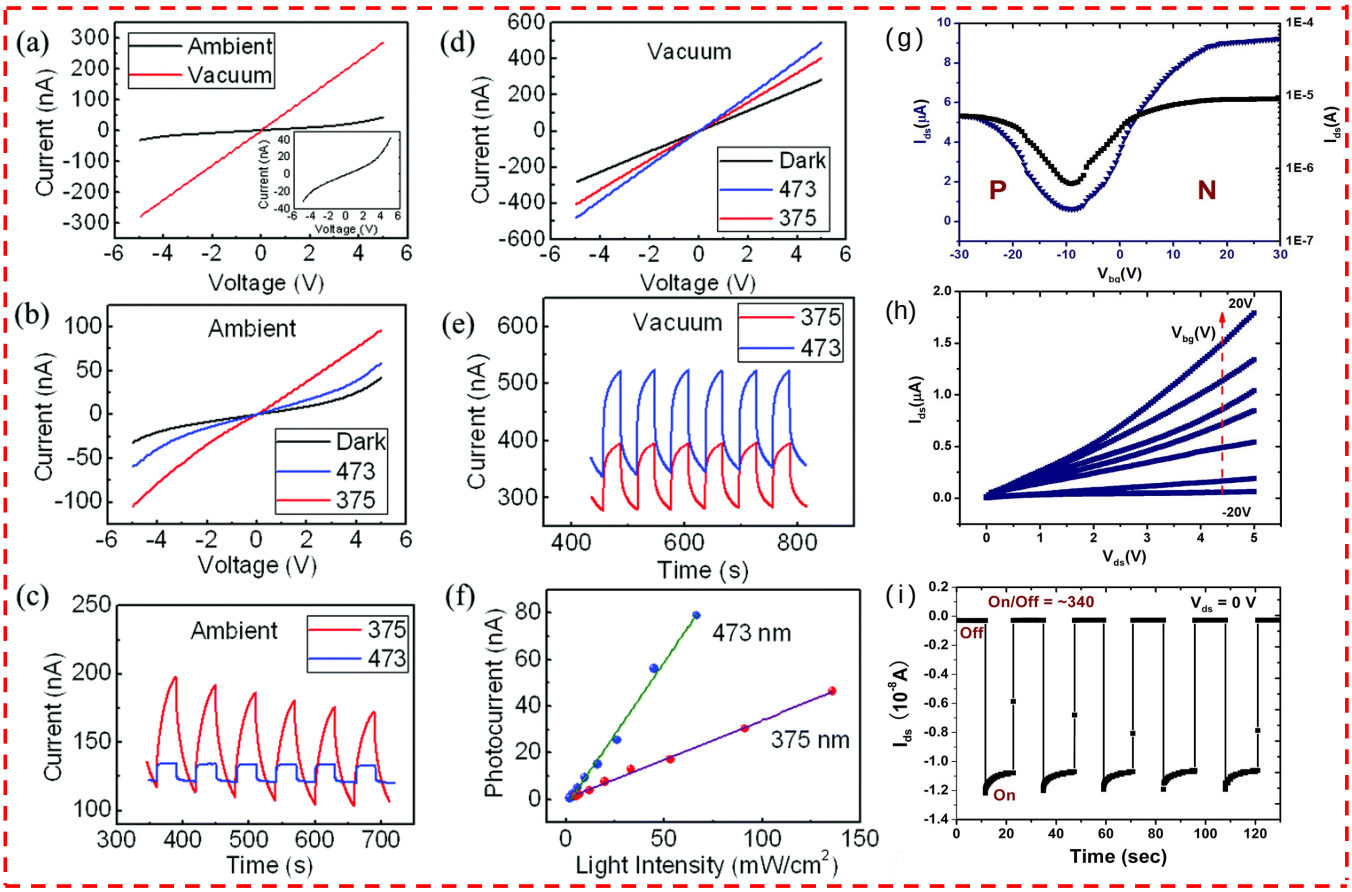

Figure 13: a) I-V curves of GaTe devices measured by the two-terminal method under vacuum (7×10^{-5} Torr) and ambient conditions. b,d) With 375 nm (power intensities of 163.9 mW cm^{-2}) and 473 nm (power intensities of 80.5 mW cm^{-2}) laser illumination, I-V curve for the same device under ambient (b) and vacuum (d) conditions in the dark. c,e) Time-resolved photoresponse of the GaTe device recorded by alternately turning the laser on and off in (c) ambient and (e) vacuum conditions. f) The functional relationship between light intensity and photocurrent with illumination of 473 and 375 nm lasers. The bias for c, e, and f is 5 V.[114] Copyright 2015, American Chemical Society. g) Transfer characteristics of GaTe-MoS_2 transistors (measured with V_{ds} = 15 V, V_{bg} = −30–30 V). H) output characteristics of GaTe-MoS_2 transistors (measured with V_{ds} = 0–5 V ,V_{bg} = −20–20 V). i) Self-driven photoswitch behavior of GaTe-MoS_2 photodetector (V_{ds} = 0 V).[115] Copyright 2016, American Chemical Society.

prolonged irradiation, which may be caused by the laser heating effect on the processes of adsorption and desorption for surface gas molecules. On the other hand, the slow O_2-doped GaTe process of the 375 nm laser resulted in the 375 nm laser exhibiting slower photoresponse kinetics. Meanwhile, the electrical contact was improved for the 375 nm laser, while it was not the case for the 473 nm laser. As shown in Figures 13d and e, the performance of the device in vacuum is better than it in the ambient environment. The vacuum-treated device shows good response linearity and synchronous photocurrent switching speed for both types of light. The PET-based flexible detector was bent several hundred times under vacuum, but it still shows a good photocurrent profile and photocurrent switching speed, which indicates the high stability of the device.

For GaTe heterojunction photodetectors, GaTe-InSe,[117] GaTe/Sn:CdS,[118] and GaTe-MoS_2[115] are commonly used. A large number of experiments have been conducted to observe the transfer curves of GaTe 2D nanosheets in those devices with the characteristics of *p*-type semiconductor,[117, 118, 115] and there is no exception in GaTe-InSe heterojunctions are no exception.[117] The I_{ds}-V_{ds} curves of GaTe-InSe p-n junctions show a full photoresponse and photovoltaic effect for illumination intensities (P_{opt}) from 0.16 mW cm^{-2} to 6.35 mW cm^{-2} in the 405 nm laser irradiation experiments. Moreover, the short-circuit current (I_{sc}) is linearly correlated with P_{opt}, showing an excellent photoresponse performance. More importantly, the GaTe-InSe heterojunction is capable of the self-powered photoresponse. Additionally, the increase of light-generated carriers results in the fact that I_{ph} increases with P_{opt}. The corresponding EQE of 4.3% for zero bias voltage operation exceeds that of many other photodetectors. In terms of photoresponse, GaTe-InSe achieves an impressive photoresponse time of about 20 μs, which is a good performance among existing photodetectors.

Unlike GaTe-InSe, GaTe/Sn:CdS is the rare coupling of nanosheet and nanowire materials,[118] but such coupling does not affect how the device performs. Instead, GaTe/Sn:CdS shows an excellent response to white light. Consistent with what was mentioned previously, the GaTe and Sn:CdS exhibit the features of *p*-type and n-type transmission properties, respectively. The GaTe/Sn:CdS hybrid heterostructure shows a sharp increase in both forward and reverses photocurrents under white light irradiation at 1 W power. Moreover, the sum of the photocurrent enhancement of GaTe and Sn:CdS is smaller compared to the photocurrent enhancement in GaTe/Sn:CdS. In addition, the photocurrent level remains almost unchanged in dozens of cycles, and it shows better reversibility and stability than separate GaTe or Sn:CdS materials. The rise and reset times are no more than 260 ms and 267 ms, respectively. Moreover, both the forward-biased and reverse-biased on-off ratios (100 and 3000) are tens or hundreds of times higher than GaTe or Sn:CdS alone (about 5), thus reflecting the exceptional heterojunction photodetector performance. The peculiar properties of GaTe/Sn:CdS heterojunction materials result from the adsorption/desorption mechanisms of surface molecular oxygen on the electrical transport behavior of GaTe/Sn:CdS heterojunctions and the effects of light modulation under forward and reverse bias.

The last heterostructures to be presented, GaTe-MoS_2,[115] differs from the previous heterostructures as GaTe-MoS_2 is coupled with high quality through vdW interactions, which eliminates the difficulty in material selection due to lattice matching. A non-monotonic *p*-*n* bipolar transport is observed on GaTe-MoS_2 by applying a positive $V_{ds} = 15$ V gate voltage at room temperature. In the transfer curves (Figure 13g), the gate-induced holes are dominant in GaTe when $V_{bg} \leq -10$ V and make contributions to the *p*-type conductivity of the heterostructure. In contrast, the electrons in MoS_2 induce *n*-type behavior at $V_{bg} \geq -10$ V. The output characteristics at varying V_{bg} demonstrate that the output current and V_{ds} are positively correlated (see Figure 13h). The source-drain current (I_{ds}) images for different source-drain bias voltages V_{ds} under light illumination can be observed under the laser illumination of 633 nm. It can be found out that the photocurrent switching ratio under reverse bias is larger than that under forward bias, and it is apparent that the GaTe-MoS_2 heterostructure has high stability and reproducibility for the photoresponse. Notably, the GaTe-MoS_2 photodetector is also capable of sub-driven photoresponse capability. The light produces a large number of electron-hole pairs at zero-bias voltage, which can be effectively separated by the inbuilt potential in the *p*-*n* heterojunction. Electrons and holes accumulate in MoS_2 and GaTe, respectively, thus generating an open-circuit voltage. When the heterojunction is in operation under short-circuit conditions, the inbuilt potential drives the photogenerated electrons and

holes, which not only generates a short-circuit current but also leads to the occurrence of efficient electron-hole separation and self-driven optical switching. When V_{ds} is set to 0 V, the photocurrent on-off ratio reaches a level that is ∼340 (see Figure 13i) greater than individual GaTe (∼10) and MoS_2 (∼85). At the same time, the EQE at this point can even reach 266%.[117] Hence, this GaTe-MoS_2 heterostructure has a massive potential of applications in some photovoltaic devices, sensitive photoswitches, and highly efficient self-driven photodetectors.

4 Summmary and outlook

Since the structure of tellurene was successfully predicted by the first principles in 2017,[31] there have been more and more researchers paying attention to the superiority of tellurene and tellurides, such as piezoelectricity,[28] high carrier mobility,[43, 44, 45] tunable narrow bandgap,[34] and high signal-to-noise ratios,[82] *etc.* Herein, we have reviewed the researches on the electronic and optical properties of tellurene, as well as the applications in photodetectors based on tellurene/tellurides ($MoTe_2$, $PdTe_2$, $PtTe_2$, WTe_2, GeTe, SnTe, GaTe) in recent years. Compared with other 2D material-based photodetectors, Te-based photodetectors have better signal-to-noise ratio,[82] faster time response or higher frequency response,[31] better flexibility,[46] and so on. These excellent properties have necessitated the applications of Te-based broadband photodetectors in a wide range.

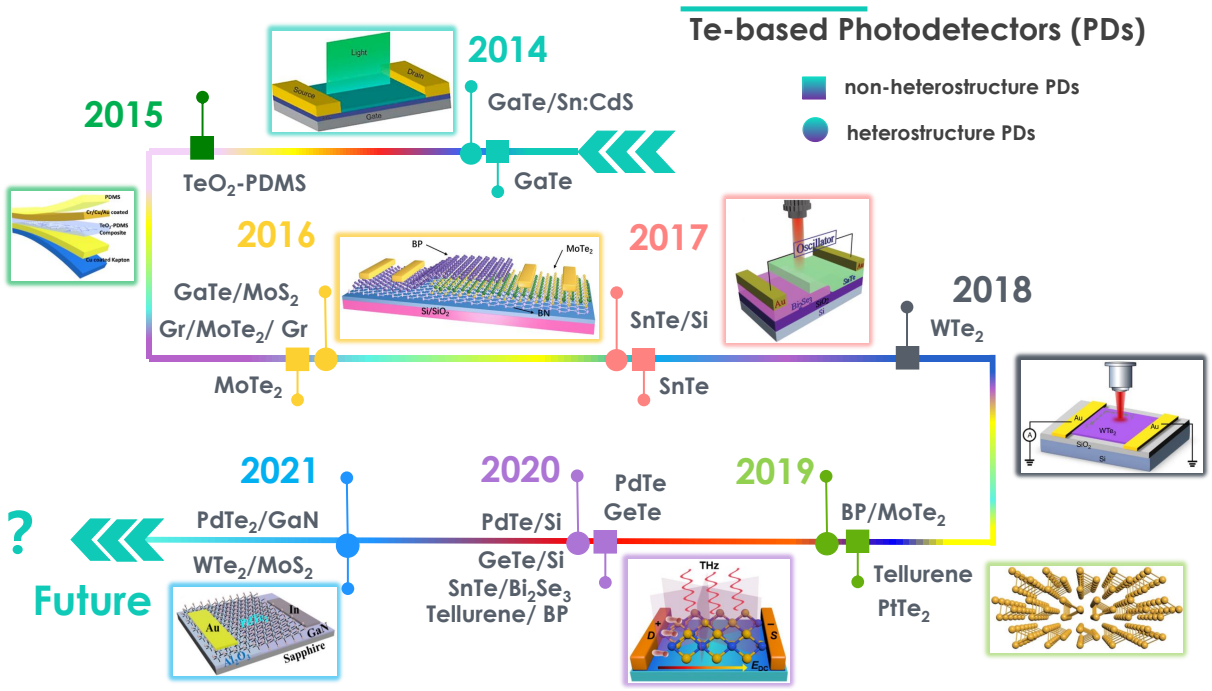

Figure 14: Timelines of Te-based photodetectors. Pictures from [113, 127, 88, 104, 128, 65, 91, 72].

Te has a thickness-dependent bandgap ranging from 1.17 eV (bilayer Te) to 0.31 eV (bulk Te). The diversity of Te leads to the multivalent properties of Te atoms with different layers. The center layer Te behaves like a metal while the outer-layer Te behaves like a semiconductor, which may be attributed to the different coordination numbers of different Te atoms. The high carrier mobility of tellurene ranges from 0.05–2.09×10^3 $cm^2V^{-1}s^{-1}$ (for electron) and 0.45–1.98×10^3 $cm^2V^{-1}s^{-1}$ (for hole), while β-Te has a zigzag direction anisotropy of electron and hole mobility. The spin-orbit coupling of Te induces the transition from the indirect to the direct bandgap, which significantly improves its light adsorption performance and expands its application in the field of optoelectronics.[31] In addition, Zhu *et al.* found out that the band structure of Te and the effective mass of electrons will change significantly under a compressive strain of -2%—10%.[64] The direct bandgap will be transformed into an indirect bandgap and the effective mass of electrons is also significantly greater compared to the unstrained case.

Table 2: Photodetectors of Te-based materials

Materials	Wavelength	R [A/W]	Bias [V]	D* [Jones]	EQE [%]	Time	Ref.
	520 nm	383	$V_g = 5$, $V_{ds} = 1$			0.6 ms	
Tellurene	1.55 μm	19.2 mA/W	$V_g = 100$, $V_{ds} = 1$		1.52	9.5 ns	[38]
	3.39 μm	18.9 mA/W	$V_g = 5$, $V_{ds} = 1$		0.66	10 ms	
Te nanosheets	261–405 nm	6.5×10^4	3	3.7×10^8	2.26×10^6	2–5 s	[119]
$MoTe_2/MoS_2$	550–1550 nm	46 mA/W	0	1.06×10^8		25–60 μs	[120]
2H-$MoTe_2/MoS_2$	200–1100 nm	4.71 (1100 nm) 4.67 (300 nm)	2		532 1935		[121]
$MoTe_2$/BP		0.2			48.10	2–4 ms	[88]
G/$MoTe_2$/G[1]	473 nm	87		10^{12}	229		[122]
p-$MoTe_2$/n-MoS_2	450–980 nm	146 mA/W (520 nm)	$V_{ds} = 0$	$>10^{10}$		~172 μs	[123]
$PdTe_2$	1–7.5 mm (0.04–0.3 THz)	10	0			1 μs	[91]
$PdTe_2$/GaN	DUV	168.5 mA/W 254.6 mA/W	0 -1	5.3×10^{12}			[72]
$PtTe_2$	200–1650 nm	0.406 (980 nm)	<-0.2	3.62×10^{12}	32.10	7.5–36.7 μs	[92]
$PtTe_2$/Si	625 nm	0.213	>0	2.66×10^{13}	42.20	~1 μs	[124]
WTe_2/graphene	650 nm	~8.7	0.5		165		[96]
WTe_2/MoS_2	400–1050 nm	31.1 (400 nm) 0.18 (1050 nm)	1	4.36×10^{10} 2.5×10^8	9460 21	<0.6 s	[97]
GeTe/Si	300–1500 nm	6-15 (850 nm)	0.1	$1–8\times10^{11}$		132–136 ms	[125]
GeTe nanofilm	600–900 nm	~100 (850 nm)	>0.5	$\sim10^{13}$			[103]
SnTe nanosheets	254–4650 nm	4.17–49.03	1			0.21–0.73 s	[106]
SnTe nanoplates	980 nm	698 mA/W	0	3.89×10^8	88.50	0.6–1.45 s	[126]
SnTe/Bi_2Se_3	300–2000 nm	0.146	5	1.15×10^{10}		6.9–19.2 μs	[104]
	1064 nm	2.36 mA/W		1.5×10^{14}	276		
SnTe/Si	1310 nm	1.15 mA/W	0	7.53×10^{10}	0.1091	2.2–3.8 μm	[105]
	1550 nm	0.18 mA/W		1.17×10^{10}	0.0144		
GaTe nanosheets	375, 475 nm	0.03	5	10^{12}	8	54 ms	[114]
GaTe-InSe	405 nm	13.8 mA/W	0		4.20	20 μs	[117]
GaTe/Sn:CdS	350–710 nm	607	2			<267 ms	[118]
GaTe/MoS_2	532 nm	1.365	5		266	6 ms	[115]

[1] G:Graphene

In terms of optics, the tellurene exhibits a response that matches its electrical properties. First of all, the energy band that changes with the decrease of layers and the occurrence of phase change makes the Raman peak of the tellurene appear to be significantly shifted significantly in fewer layers. It also makes tellurene materials with different layers and different phases show different degrees of absorption for the different wavelengths of light, which provides more possibilities and a wider scope pof applications in tellurene-based photodetectors. At the same time, the tellurene energy band will also be affected by strain, which enables the relevant detection devices to achieve interesting light response performance. Moreover, the narrow bandgap of tellurene determines its richness in terms of photoresponse, including photovoltaic effect and photoelectric effect, *etc.*

The emerging studies on Te in the last few years have provided new ideas for manufacturing Te-based photodetectors. The advantages of 2D Te, for example, large-scale preparation,[32] environmental stability,[27, 31, 33] and tunable bandgap,[34] improve the performance of Te-based photodetectors and expand their scope of applications significantly. Many researchers have found out that tellurene/tellurides (such as $MoTe_2$, $PdTe_2$, $PtTe_2$, WTe_2, GeTe, SnTe, GaTe, *etc.*) can be stacked with other 2D materials to form heterostructures.[72, 73, 115, 96] They can help reduce the barrier to application for Te and improve the detection performance to some extent. For example, the $WSe_2/MoTe_2$ heterojunction photodetector itself eliminates need for lattice matching through van der Waals force coupling and ensures the ultra-high sensitive detection of infrared wavelengths.[129, 130] In addition, such PTE photodetectors as SnTe rely on gapless surface states and narrow bulk bandgap to enable the built-in electric field derived from the photothermal temperature gradient, thus spontaneously driving the device to work. This kind of photodectors can respond to an ultra-wide spectrum from 404 nm to 10.6 μm while maintaining a low dark current and a high current switching ratio of 10^5.[74]

There remain some drawbacks in respect of improvement to the development of 2D Te photodetectors. For instance, the large-area preparation of simple substance Te is a challenge to address in the future and weak light absorption is one of the major constraints on the photoresponsivity of monolayer Te detectors. Likewise, the direct bandgap property makes light absorption efficiency appears only in monolayer structures for Te devices. Additionally, the electrical and optoelectronic properties of atomically thin 2D layered materials are easily affected by environmental conditions. Some 2D materials, especially the narrow bandgap materials such as b-P and b-AsP, are unstable in ambient air. Furthermore, the large dark current which would cause the low signal-to-noise ratio for the photoconductive 2D photodetectors could be induced, thus resulting in low specific detectivity. Meanwhile, the large scale material deposition of high quality tellurene/tellurides films with high reliability and low variability is of great significance. For these problems, some solutions are suggested as following:

1. To enhance the outcome of infrared light absorption, the 2D materials with multiple layers instead of a single layer could be selected.

2. To reduce the impact of dark current, the 2D materials with superior tunability performance can be selected to ensure their thickness is neither too thick nor too thin, so that the dark current can be suppressed by applying gate voltage. In addition to the tuning of electric field, such hybrid structures as lateral *p-n* junction are also preferred.

3. To form heterojunctions by combining tellurides with other 2D materials or bulk materials can be a promising method (As illustrated in Table2). The heterojunction not only addresses the defects of the material itself in the light detection range, but also enables the large-scale preparation of compound materials, which also provides a guidance strategy for the application of 2D materials in the future.

4. It is also worth noting that only two of the three phases of Te have been widely studied, while γ-Te has drawn little attention because of its metastability. In fact, however, although many materials require extreme working environment, they may lead to unexpected physical properties and play a role in new fields.

Especially for 2D tellurene/tellurides and their heterostructures-based broadband photodetectors, many studies are focused on visible to mid-IR broadband compared with ultraviolet to mid-IR ultra-broadband

that is preferred in devices and need more explorations. Additionally, the mechanism of the transport and carrier dynamics are still not explored clearly enough for such photodetectors compared with those based on BP and TMDCs, thus calling for more investigations. Moreover, to further enhance the properties of such photodetectors, it is of significance to improve the materials fabrication procedure, ultra-thin 2D tellurene/tellurides can be produced by PVD strategy. Nevertheless, the demands of a high-purity atomic source and high vacuum environment constrain the possibility of amplification to restrict the potential for upscaling. LPE technology is an effective means to fabricate layered 2D Te nanostructures, yet the inefficient control of derived materials thickness and the small scale limit further steps. In addition, *in-situ* CVD has been applied to many other 2D materials, but there are fewer reports on the preparation of ultra-thin 2D tellurene/tellurides. Hence, the development of CVD technology to grow atomic thin Te materials is necessary. Particularly, the precisely controllable preparation for doping and Te-based heterojunctions should be highly sought after.

Actually, the applications of the 2D Te-based photodetectors are relatively rough at present, and does not give full play to the full potential strength of such materials. It has to be said that in recent years, the theoretical researches on the properties of tellurene and tellurides have greatly promoted its development in applications. It is worth mentioning that although the publications on tellurene and tellurides have soared in recent years, there is still a lack of in-depth theoretical researches on various properties of tellurides. In the future, it can be expected to see more theoretical works on tellurides, and the application of modulation methods may bring unprecedented results to the properties of tellurides, such as doping, strain, stacking, and heterostructure, *etc.* These approaches may trigger experimental attempts to develop performance-enhanced photodetectors. Most significantly, corresponding detectors should develop towards heterojunction and large-area array in order to be better commercialized and industrialized. Although we have gained a certain understanding of Te-based materials, this is still a very open and promising field. It is certain that the collision between theoretical and experimental efforts will lead to the development of more advanced Te-based photodectors with a better performance and a wider scope of applications in the future.

Acknowledgements

Funding: The authors acknowledge the support from Songshan Lake Materials Laboratory, China (No. Y0D1051F211). Cai S. H. acknowledges support from the Hong Kong Polytechnic University (No. 1-BQ96), and the General Research Fund (No. 15306021) from the Hong Kong Research Grant Council and the open subject of National Laboratory of Solid State Microstructures, Nanjing University (M34001). Yan Z. H. acknowledges the support from Jiangsu Students' Innovation and Entrepreneurship Training Program (No. 202111117008Z).

References

[1] K. S. Novoselov, A. K. Geim, S. V. Morozov, D.-e. Jiang, Y. Zhang, S. V. Dubonos, I. V. Grigorieva, A. A. Firsov, *science* **2004**, *306*, 5696 666.

[2] H. Xie, M. Hu, H. Bao, *Appl. Phys. Lett.* **2014**, *104*, 13 131906.

[3] A. Nijamudheen, R. Bhattacharjee, S. Choudhury, A. Datta, *J. Phys. Chem. C* **2015**, *119*, 7 3802.

[4] A. Carvalho, M. Wang, X. Zhu, A. S. Rodin, H. Su, A. H. C. Neto, *Nat. Rev. Mater.* **2016**, *1*, 11 1.

[5] B. Peng, H. Zhang, H. Shao, Y. Xu, R. Zhang, H. Zhu, *J. Mater. Chem. C* **2016**, *4*, 16 3592.

[6] J.-M. Lehn, *Angew. Chem. Int. Ed.* **2015**, *54*, 11 3276.

[7] C. J. Kloxin, C. N. Bowman, *Chem. Soc. Rev.* **2013**, *42*, 17 7161.

[8] R. J. Wojtecki, M. A. Meador, S. J. Rowan, *Nat. Mater.* **2011**, *10*, 1 14.

[9] Y. Zhang, Y. Qi, S. Ulrich, M. Barboiu, O. Ramström, *Mater. Chemi. Front.* **2020**, *4*, 2 489.

[10] J. Dahlke, S. Zechel, M. D. Hager, U. S. Schubert, *Adv. Mater. Inter.* **2018**, *5*, 17 1800051.

[11] S. Lin, W. K. Lai, Y. Li, W. Lu, G. Bai, S. P. Lau, *SmartMat* **2021**.

[12] I. Ali, X. Mbianda, A. Burakov, E. Galunin, I. Burakova, E. Mkrtchyan, A. Tkachev, V. Grachev, et al., *Environ. Int.* **2019**, *127* 160.

[13] Y. Bai, T. Xu, X. Zhang, *Micromachines* **2020**, *11*, 1 60.

[14] J. Peña-Bahamonde, H. N. Nguyen, S. K. Fanourakis, D. F. Rodrigues, *J. Nanobiotechnol.* **2018**, *16*, 1 1.

[15] S. Stankovich, D. A. Dikin, G. H. Dommett, K. M. Kohlhaas, E. J. Zimney, E. A. Stach, R. D. Piner, S. T. Nguyen, R. S. Ruoff, *Nature* **2006**, *442*, 7100 282.

[16] M. Sang, J. Shin, K. Kim, K. J. Yu, *Nanomaterials* **2019**, *9*, 3 374.

[17] J. W. Suk, R. D. Piner, J. An, R. S. Ruoff, *ACS nano* **2010**, *4*, 11 6557.

[18] T. Chowdhury, E. C. Sadler, T. J. Kempa, *Chem. Rev.* **2020**, *120*, 22 12563.

[19] X. Yin, C. S. Tang, Y. Zheng, J. Gao, J. Wu, H. Zhang, M. Chhowalla, W. Chen, A. T. Wee, *Chem. Soc. Rev.* **2021**.

[20] W. Choi, N. Choudhary, G. H. Han, J. Park, D. Akinwande, Y. H. Lee, *Mater. Today* **2017**, *20*, 3 116.

[21] N. Mao, J. Tang, L. Xie, J. Wu, B. Han, J. Lin, S. Deng, W. Ji, H. Xu, K. Liu, et al., *J. Am. Chem. Soc.* **2016**, *138*, 1 300.

[22] J. Kim, S. S. Baik, S. H. Ryu, Y. Sohn, S. Park, B.-G. Park, J. Denlinger, Y. Yi, H. J. Choi, K. S. Kim, *Science* **2015**, *349*, 6249 723.

[23] Q. Guo, A. Pospischil, M. Bhuiyan, H. Jiang, H. Tian, D. Farmer, B. Deng, C. Li, S.-J. Han, H. Wang, et al., *Nano lett.* **2016**, *16*, 7 4648.

[24] X. Ling, H. Wang, S. Huang, F. Xia, M. S. Dresselhaus, *Proc. Natl. Acad. Sci.* **2015**, *112*, 15 4523.

[25] X. Wang, A. M. Jones, K. L. Seyler, V. Tran, Y. Jia, H. Zhao, H. Wang, L. Yang, X. Xu, F. Xia, *Nat. Nanotechnol.* **2015**, *10*, 6 517.

[26] H. Yuan, X. Liu, F. Afshinmanesh, W. Li, G. Xu, J. Sun, B. Lian, A. G. Curto, G. Ye, Y. Hikita, et al., *Nat. Nanotechnol.* **2015**, *10*, 8 707.

[27] J. D. Wood, S. A. Wells, D. Jariwala, K.-S. Chen, E. Cho, V. K. Sangwan, X. Liu, L. J. Lauhon, T. J. Marks, M. C. Hersam, *Nano lett.* **2014**, *14*, 12 6964.

[28] T. I. Lee, S. Lee, E. Lee, S. Sohn, Y. Lee, S. Lee, G. Moon, D. Kim, Y. S. Kim, J. M. Myoung, et al., *Adv. Mater.* **2013**, *25*, 21 2920.

[29] U. Coscia, G. Ambrosone, M. Palomba, S. Binetti, A. Le Donne, D. Siliqi, G. Carotenuto, *Appl. Surf. Sci.* **2018**, *457* 229.

[30] G. Zhang, H. Fang, H. Yang, L. A. Jauregui, Y. P. Chen, Y. Wu, *Nano lett.* **2012**, *12*, 7 3627.

[31] Z. Zhu, X. Cai, S. Yi, J. Chen, Y. Dai, C. Niu, Z. Guo, M. Xie, F. Liu, J.-H. Cho, et al., *Phys. Rev. Lett.* **2017**, *119*, 10 106101.

[32] Y. Wang, G. Qiu, R. Wang, S. Huang, Q. Wang, Y. Liu, Y. Du, W. A. Goddard, M. J. Kim, X. Xu, et al., *Nat. Electron.* **2018**, *1*, 4 228.

[33] B. Wu, X. Liu, J. Yin, H. Lee, *Mater. Res. Express* **2017**, *4*, 9 095902.

[34] J. Qiao, Y. Pan, F. Yang, C. Wang, Y. Chai, W. Ji, *Sci. Bull.* **2018**, *63*, 3 159.

[35] Z. Gao, F. Tao, J. Ren, *Nanoscale* **2018**, *10*, 27 12997.

[36] J. Yao, G. Yang, *Nanoscale* **2020**, *12*, 2 454.

[37] S. C. Dhanabalan, J. S. Ponraj, H. Zhang, Q. Bao, *Nanoscale* **2016**, *8*, 12 6410.

[38] C. Shen, Y. Liu, J. Wu, C. Xu, D. Cui, Z. Li, Q. Liu, Y. Li, Y. Wang, X. Cao, et al., *ACS nano* **2019**, *14*, 1 303.

[39] Z. Shi, R. Cao, K. Khan, A. K. Tareen, X. Liu, W. Liang, Y. Zhang, C. Ma, Z. Guo, X. Luo, et al., *Nanomicro Lett.* **2020**, *12*, 1 1.

[40] J. Peng, Y. Pan, Z. Yu, J. Wu, J. Wu, Y. Zhou, Y. Guo, X. Wu, C. Wu, Y. Xie, *Angew. Chem. Int. Ed.* **2018**, *57*, 41 13533.

[41] A. Londoño-Calderon, D. J. Williams, C. Ophus, M. T. Pettes, *Small* **2020**, *16*, 49 2005447.

[42] Q. Wang, M. Safdar, K. Xu, M. Mirza, Z. Wang, J. He, *ACS nano* **2014**, *8*, 7 7497.

[43] W. Zhou, J. Chen, H. Gao, T. Hu, S. Ruan, A. Stroppa, W. Ren, *Adv. Mater.* **2019**, *31*, 5 1804629.

[44] X. Qian, L. Fu, J. Li, *Nano Res.* **2015**, *8*, 3 967.

[45] L. Yin, X. Zhan, K. Xu, F. Wang, Z. Wang, Y. Huang, Q. Wang, C. Jiang, J. He, *Appl. Phys. Lett.* **2016**, *108*, 4 043503.

[46] W. Yu, S. Li, Y. Zhang, W. Ma, T. Sun, J. Yuan, K. Fu, Q. Bao, *Small* **2017**, *13*, 24 1700268.

[47] L. Zeng, D. Wu, J. Jie, X. Ren, X. Hu, S. P. Lau, Y. Chai, Y. H. Tsang, *Adv. Mater.* **2020**, *32*, 52 2004412.

[48] D. K. Sang, B. Wen, S. Gao, Y. Zeng, F. Meng, Z. Guo, H. Zhang, *Nanomaterials* **2019**, *9*, 8 1075.

[49] J. Qiao, X. Kong, Z.-X. Hu, F. Yang, W. Ji, *Nat. Commun.* **2014**, *5*, 1 1.

[50] Z.-X. Hu, X. Kong, J. Qiao, B. Normand, W. Ji, *Nanoscale* **2016**, *8*, 5 2740.

[51] Y. Zhao, J. Qiao, P. Yu, Z. Hu, Z. Lin, S. P. Lau, Z. Liu, W. Ji, Y. Chai, *Adv. Mater.* **2016**, *28*, 12 2399.

[52] Y. Zhao, J. Qiao, Z. Yu, P. Yu, K. Xu, S. P. Lau, W. Zhou, Z. Liu, X. Wang, W. Ji, et al., *Adv. Mater.* **2017**, *29*, 5 1604230.

[53] P. Grosse, In *Die Festkörpereigenschaften von Tellur*, 1–204. Springer, **1969**.

[54] W. Yang, Z. Yan, K. Zhang, W. Wang, S. Lei, S. Zeng, Y. Tu, *Surface Science* **2021**, *714* 121919.

[55] Z. Yan, W. Yang, H. Yang, C. Ji, L. Zhao, S. Zeng, Y. Tu, *arXiv preprint arXiv:2109.13575* **2021**.

[56] C. Si, Z. Sun, F. Liu, *Nanoscale* **2016**, *8*, 6 3207.

[57] W. Bao, L. Jing, J. Velasco, Y. Lee, G. Liu, D. Tran, B. Standley, M. Aykol, S. Cronin, D. Smirnov, et al., *Nature Phys.* **2011**, *7*, 12 948.

[58] Y. Wang, Z. Ni, L. Liu, Y. Liu, C. Cong, T. Yu, X. Wang, D. Shen, Z. Shen, *ACS nano* **2010**, *4*, 7 4074.

[59] H. Fu, J. Zhang, Z. Ding, H. Li, S. Meng, *Appl. Phys. Lett.* **2014**, *104*, 13 131904.

[60] J. Kang, A. Hirata, L. Kang, X. Zhang, Y. Hou, L. Chen, C. Li, T. Fujita, K. Akagi, M. Chen, *Angew. Chem. Int. Ed.* **2013**, *52*, 6 1664.

[61] Y. Dong, B. Zeng, X. Zhang, D. Li, J. He, M. Long, *J. Appl. Phys.* **2019**, *125*, 6 064304.

[62] H. Ma, W. Hu, J. Yang, *Nanoscale* **2019**, *11*, 45 21775.

[63] Y. Xiang, S. Gao, R.-G. Xu, W. Wu, Y. Leng, *Nano Energy* **2019**, *58* 202.

[64] Z. Zhu, C. Cai, C. Niu, C. Wang, Q. Sun, X. Han, Z. Guo, Y. Jia, *arXiv preprint arXiv:1605.03253* **2016**.

[65] S. Gao, C. Sun, X. Zhang, *Nanophotonics* **2020**, *9*, 7 1931.

[66] T. Tang, F. Zhang, M. Wang, Z. Wang, X. Xu, *Chin. Opt. Lett.* **2020**, *18*, 4 041403.

[67] W. Huang, Y. Zhang, Q. You, P. Huang, Y. Wang, Z. N. Huang, Y. Ge, L. Wu, Z. Dong, X. Dai, et al., *Small* **2019**, *15*, 23 1900902.

[68] Y. Wang, G. Qiu, R. Wang, S. Huang, Q. Wang, Y. Liu, Y. Du, W. A. Goddard, M. J. Kim, X. Xu, et al., *Nat. Electron.* **2018**, *1*, 4 228.

[69] Y. Du, G. Qiu, Y. Wang, M. Si, X. Xu, W. Wu, P. D. Ye, *Nano lett.* **2017**, *17*, 6 3965.

[70] Y. Wang, Y. Wang, Y. Dong, L. Zhou, H. Wei, M. Long, S. Xiao, J. He, *Nanoscale* **2021**, *13*, 37 15882.

[71] R. Han, M. Qi, Z. Mao, X. Lin, P. Wu, *Appl. Surf. Sci.* **2021**, *541* 148454.

[72] Y. Liang, M. Ma, X. Zhong, C. Xie, X. Tong, K. Xing, C. Wu, *IEEE Electron Device Lett.* **2021**.

[73] H. Xu, C. Guo, J. Zhang, W. Guo, C.-N. Kuo, C. S. Lue, W. Hu, L. Wang, G. Chen, A. Politano, et al., *Small* **2019**, *15*, 52 1903362.

[74] H. Liu, Y. Liu, S. Dong, H. Xu, Y. Wu, L. Hao, B. Cao, M. Li, Z. Wang, Z. Han, et al., *ACS Appl. Mater. Interfaces* **2020**, *12*, 44 49830.

[75] M. Long, P. Wang, H. Fang, W. Hu, *Adv. Funct. Mater.* **2019**, *29*, 19 1803807.

[76] O. V. Misochko, T. Dekorsy, S. V. Andreev, V. Kompanets, Y. A. Matveets, A. Stepanov, S. V. Chekalin, *Appl. Phys. Lett.* **2007**, *90*, 7 071901.

[77] D. Souilhac, D. Billerey, A. Gundjian, *Appl. Opt.* **1990**, *29*, 12 1798.

[78] M. Panahi-Kalamuei, P. Rajabpour, M. Salavati-Niasari, Z. Zarghami, M. Mousavi-Kamazani, *J. Mater. Sci. Mater. Electron.* **2015**, *26*, 6 3691.

[79] D. Tsiulyanu, S. Marian, V. Miron, H.-D. Liess, *Sens. Actuat. B Chem.* **2001**, *73*, 1 35.

[80] J.-W. Liu, J.-H. Zhu, C.-L. Zhang, H.-W. Liang, S.-H. Yu, *J. Am. Chem. Soc.* **2010**, *132*, 26 8945.

[81] H. Tao, H. Liu, D. Qin, K. Chan, J. Chen, Y. Cao, *J. Nanosci. Nanotechnol.* **2010**, *10*, 12 7997.

[82] S. Deckoff-Jones, Y. Wang, H. Lin, W. Wu, J. Hu, *ACS Photonics* **2019**, *6*, 7 1632.

[83] D. K. Sang, T. Ding, M. N. Wu, Y. Li, J. Li, F. Liu, Z. Guo, H. Zhang, H. Xie, *Nanoscale* **2019**, *11*, 39 18116.

[84] M. M. Furchi, A. Pospischil, F. Libisch, J. Burgdörfer, T. Mueller, *Nano lett.* **2014**, *14*, 8 4785.

[85] F. Wang, Z. Wang, K. Xu, F. Wang, Q. Wang, Y. Huang, L. Yin, J. He, *Nano lett.* **2015**, *15*, 11 7558.

[86] Y. Fu, M. Long, A. Gao, Y. Wang, C. Pan, X. Liu, J. Zeng, K. Xu, L. Zhang, E. Liu, et al., *Appl. Phys. Lett.* **2017**, *111*, 4 043502.

[87] A. Pezeshki, S. H. H. Shokouh, T. Nazari, K. Oh, S. Im, *Adv. Mater.* **2016**, *28*, 16 3216.

[88] Y. Xie, E. Wu, J. Zhang, X. Hu, D. Zhang, J. Liu, *ACS Appl. Mater. Interfaces* **2019**, *11*, 15 14215.

[89] W. Chen, R. Liang, S. Zhang, Y. Liu, W. Cheng, C. Sun, J. Xu, *Nano Res.* **2020**, *13*, 1 127.

[90] B. G. Streetman, S. Banerjee, et al., *Solid state electronic devices*, volume 10, Pearson/Prentice Hall Upper Saddle River, NJ, **2006**.

[91] C. Guo, Y. Hu, G. Chen, D. Wei, L. Zhang, Z. Chen, W. Guo, H. Xu, C.-N. Kuo, C. S. Lue, et al., *Sci. Adv.* **2020**, *6*, 36 eabb6500.

[92] X.-W. Tong, Y.-N. Lin, R. Huang, Z.-X. Zhang, C. Fu, D. Wu, L.-B. Luo, Z.-J. Li, F.-X. Liang, W. Zhang, *ACS Appl. Mater. Interfaces* **2020**, *12*, 48 53921.

[93] L. Viti, D. Coquillat, A. Politano, K. A. Kokh, Z. S. Aliev, M. B. Babanly, O. E. Tereshchenko, W. Knap, E. V. Chulkov, M. S. Vitiello, *Nano lett.* **2016**, *16*, 1 80.

[94] M. S. Shawkat, S. B. Hafiz, M. M. Islam, S. A. Mofid, M. M. Al Mahfuz, A. Biswas, H.-S. Chung, E. Okogbue, T.-J. Ko, D. Chanda, et al., *ACS Appl. Mater. Interfaces* **2021**, *13*, 13 15542.

[95] E. Torun, H. Sahin, S. Cahangirov, A. Rubio, F. Peeters, *J. Appl. Phys.* **2016**, *119*, 7 074307.

[96] Y. Liu, C. Liu, X. Wang, L. He, X. Wan, Y. Xu, Y. Shi, R. Zhang, F. Wang, *Sci. Rep.* **2018**, *8*, 1 1.

[97] L. Li, G. Zhang, H. Wu, L. Yang, P. Gao, S. Zhang, X. Wen, W. Zhang, H. Chang, *J Phys. Chem. C* **2021**.

[98] N. El-Hinnawy, P. Borodulin, E. B. Jones, B. P. Wagner, M. R. King, J. S. Mason, J. Hartman, R. Howell, M. Lee, R. Young, In *CS MANTECH Conf.* **2014** 401–404.

[99] M. Wang, Y. Shim, M. Rais-Zadeh, *IEEE Electron Device Lett.* **2014**, *35*, 4 491.

[100] Z. Zheng, X. Su, R. Deng, C. Stoumpos, H. Xie, W. Liu, Y. Yan, S. Hao, C. Uher, C. Wolverton, et al., *J. Am. Chem. Soc.* **2018**, *140*, 7 2673.

[101] R. Mantovan, R. Fallica, A. M. Gerami, T. Mølholt, C. Wiemer, M. Longo, H. Gunnlaugsson, K. Johnston, H. Masenda, D. Naidoo, et al., *Sci. Rep.* **2017**, *7*, 1 1.

[102] Y. Zhao, L. Tang, S. Yang, S. P. Lau, K. S. Teng, *Nano. Res. Lett.* **2020**, *15*, 1 1.

[103] Y. Zhao, L. Tang, S. Yang, K. S. Teng, S. P. Lau, *Opt. Lett.* **2020**, *45*, 5 1108.

[104] H. Zhang, Z. Song, D. Li, Y. Xu, J. Li, C. Bai, B. Man, *Appl. Surf. Sci.* **2020**, *509* 145290.

[105] H. Zhang, B. Man, Q. Zhang, *ACS Appl. Mater. Interfaces* **2017**, *9*, 16 14067.

[106] J. Yang, W. Yu, Z. Pan, Q. Yu, Q. Yin, L. Guo, Y. Zhao, T. Sun, Q. Bao, K. Zhang, *Small* **2018**, *14*, 37 1802598.

[107] S. Murashov, V. Yarzhemsky, V. Nefedov, E. N. Murav'ev, *Russ. J. Inorg. Chem.* **2007**, *52*, 8 1243.

[108] W. Li, H. Liu, S. Wang, S. Chen, Q. Wang, *Nanoscale Res. Lett.* **2017**, *12*, 1 1.

[109] E. Mercado, Y. Zhou, Y. Xie, Q. Zhao, H. Cai, B. Chen, W. Jie, S. Tongay, T. Wang, M. Kuball, *ACS omega* **2019**, *4*, 19 18002.

[110] B. Chitara, A. Ya'akobovitz, *Nanotechnol.* **2017**, *28*, 42 42LT02.

[111] S. Siddique, C. C. Gowda, R. Tromer, S. Demiss, A. R. S. Gautam, O. E. Femi, P. Kumbhakar, D. S. Galvao, A. Chandra, C. S. Tiwary, *ACS Appl. Nano Mater.* **2021**, *4*, 5 4829.

[112] M. Bokova, A. Tverjanovich, C. J. Benmore, D. Fontanari, A. Sokolov, M. Khomenko, M. Kassem, I. Ozheredov, E. Bychkov, *ACS Appl. Mater. Interfaces* **2021**, *13*, 31 37363.

[113] F. Liu, H. Shimotani, H. Shang, T. Kanagasekaran, V. Zolyomi, N. Drummond, V. I. Fal'ko, K. Tanigaki, *ACS Nano* **2014**, *8*, 1 752.

[114] Z. Wang, M. Safdar, M. Mirza, K. Xu, Q. Wang, Y. Huang, F. Wang, X. Zhan, J. He, *Nanoscale* **2015**, *7*, 16 7252.

[115] S. Yang, C. Wang, C. Ataca, Y. Li, H. Chen, H. Cai, A. Suslu, J. C. Grossman, C. Jiang, Q. Liu, et al., *ACS Appl. Mater. Interfaces* **2016**, *8*, 4 2533.

[116] G. Yu, Z. Liu, X. Xie, X. Ouyang, G. Shen, *J. Mater. Chem. C* **2014**, *2*, 30 6104.

[117] W. Feng, Z. Jin, J. Yuan, J. Zhang, S. Jia, L. Dong, J. Yoon, L. Zhou, R. Vajtai, J. M. Tour, et al., *2D Mater.* **2018**, *5*, 2 025008.

[118] W. Zhou, Y. Zhou, Y. Peng, Y. Zhang, Y. Yin, D. Tang, *Nanotechnology* **2014**, *25*, 44 445202.

[119] R. Cao, Y. Zhang, H. Wang, Y. Zeng, J. Zhao, L. Zhang, J. Li, F. Meng, Z. Shi, D. Fan, et al., *Nanophotonics* **2020**, *9*, 8 2459.

[120] Y. Chen, X. Wang, G. Wu, Z. Wang, H. Fang, T. Lin, S. Sun, H. Shen, W. Hu, J. Wang, et al., *Small* **2018**, *14*, 9 1703293.

[121] Y. Ding, N. Zhou, L. Gan, X. Yan, R. Wu, I. H. Abidi, A. Waleed, J. Pan, X. Ou, Q. Zhang, et al., *Nano Energy* **2018**, *49* 200.

[122] F. Wang, L. Yin, Z. Wang, K. Xu, F. Wang, T. A. Shifa, Y. Huang, Y. Wen, C. Jiang, J. He, *Appl. Phys. Lett.* **2016**, *109*, 19 193111.

[123] S. Li, Z. He, Y. Ke, J. Guo, T. Cheng, T. Gong, Y. Lin, Z. Liu, W. Huang, X. Zhang, *Appl. Phys. Express* **2019**, *13*, 1 015007.

[124] M. S. Shawkat, T. A. Chowdhury, H.-S. Chung, S. Sattar, T.-J. Ko, J. A. Larsson, Y. Jung, *Nanoscale* **2020**, *12*, 45 23116.

[125] Y. Zhao, L. Tang, S. Yang, S. P. Lau, K. S. Teng, *Nanoscale Res. Lett.* **2020**, *15*, 1 1.

[126] J. Liu, X. Li, H. Wang, G. Yuan, A. Suvorova, S. Gain, Y. Ren, W. Lei, *ACS Appl. Mater. Interfaces* **2020**, *12*, 28 31810.

[127] J. M. Wu, C. C. Lee, Y. H. Lin, *Nano Energy* **2015**, *14* 102.

[128] Q. Wang, J. Zheng, Y. He, J. Cao, X. Liu, M. Wang, J. Ma, J. Lai, H. Lu, S. Jia, et al., *Nat. Commun.* **2019**, *10*, 1 1.

[129] D. Jariwala, T. J. Marks, M. C. Hersam, *Nat. Mater.* **2017**, *16*, 2 170.

[130] J. Chen, Y. Shan, Q. Wang, J. Zhu, R. Liu, *Nanotechnology* **2020**, *31*, 29 295201.